Cross-shelf exchanges in the northern Bay of Biscay

Anıl Akpınar[1,2], Guillaume Charria[1] Sébastien Theetten[1] , Frédéric Vandermeirsch[1]

1) Ifremer, Univ. Brest, CNRS, IRD, Laboratoire d'Océanographie Physique et Spatiale (LOPS), IUEM, 29280 Brest, France

2) Now at the National Oceanography Centre, Liverpool, UK

Corresponding author: Anıl Akpınar, IFREMER (akpinar.anil@gmail.com)

Submitted to:

Journal of Marine Systems

Abstract

The spatio-temporal distribution of cross-shelf exchanges in the northern Bay of Biscay from 2007 to 2010 were investigated using a high-resolution three-dimensional model as well as sea-surface temperature and chlorophyll-*a* concentration satellite observations. Our results show that the net yearly mean transport was upslope each year, with 2010 showing the highest value (0.93 Sv upslope). Bottom fluxes showed peak values near Chapel Bank, with mean values of 0.1 $m^3 s^{-1} m^{-2}$ and maximum values of 0.2 $m^3 s^{-1} m^{-2}$. Our model demonstrated that cross-shelf exchanges can be divided into three vertical layers. At the surface, cross-shelf transports are driven by wind forcing (Ekman transport accounts for about 60% of the total cross-shelf

transport) and mesoscale activity (eddy advection accounts for about 30% of transport). In the absence of mesoscale activity, Ekman transport at the surface is typically balanced out by a downslope flux at the bottom boundary layer. Exchanges at mid-depths are regulated by mesoscale activity and tides. A ubiquitous feature appeared at the bottom boundary with a cross-shelf flow in the downslope direction. Numerical simulations suggest bottom fluxes of $0.1\ m^3\ s^{-1}\ m^{-2}$, in agreement with previous *in situ* observations. We discuss the impact of winds, tides and mesoscale eddies on cross-shelf exchanges using different examples. The eddy census was obtained using an eddy-tracking algorithm. The shelf break was shown to be an important area of eddy presence due to slope current instabilities. The impact of eddies on surface and mid-depth transport is illustrated with a shelf-break eddy as an example, from its generation to dissipation and its contribution to cross-shelf exchanges. Results suggest that the largest magnitudes of downslope transports occur in the presence of both strong winds and intense eddy activity. Our detailed and quantitative exploration of cross-shelf transports in the northern Bay of Biscay highlights the relative contribution of intermittent processes (*e.g.* wind-driven events, eddies, frictional bottom layer) and confirms the complex links between the coastal and open ocean over shelf breaks.

Keywords: Cross-shelf exchanges, shelf break, mesoscale dynamics, slope current, Bay of Biscay

1. Introduction

Representing a small part of the oceans, continental shelves are the most biologically productive regions, supporting more than 90% of fish catches (Pauly et al.,2002), and creating a sink for atmospheric carbon dioxide (Gruber, 2015). One such example is the European continental shelf (Frankignoulle and Borges, 2001). The biological production, carbon and nutrient dynamics depend on the environmental conditions over the shelf, which are affected by various factors (e.g. riverine supply, atmospheric forcings). One of the key factors controlling the hydrological and biological conditions over the continental shelf is the amplitude of cross-shelf exchanges (Huthnance, 1995). Transporting nutrients, sediments, biota and materials, and regulating their delivery and removal rates on the continental shelf (Brink, 2016), cross-shelf exchanges are important for the carbon and nutrient budgets of the ocean (Huthnance et al., 2002; Holt et al., 2009; Simpson and McCandliss, 2013). However, cross-shelf exchanges remain a complex issue to address, because cross-shelf circulation is weak in intensity, not easily observed and often ageostrophic (Brink, 2016).

Various studies have investigated cross-shelf exchanges using *in situ* and satellite observations (Piola et al., 2010; Porter et al., 2016; Nencioli et al., 2016), whereas others have also included numerical approaches (Serra et al., 2010; Zhang and Gawarkiewicz, 2015). Numerous studies have focused on specific processes leading to cross-shelf exchanges, such as fronts (Nencioli et al., 2016), eddies (Peliz et al., 2004; Shapiro et al., 2010; Combes et al., 2013, Cherian and Brink., 2016; Rubio et al., 2018) or Ekman upwelling (Combes et al., 2013). Some studies have investigated the contribution of the different physical mechanisms on cross-shelf exchanges (Zhou et al.,2014; Zhou et al.,2015; Zhang et al.,2017), whereas others have investigated their influence on the ecosystem (Zhao and Guo, 2011). Still others have provided a broader perspective, quantifying cross-shelf exchanges (Graham et al., 2018) for larger domains, such

as the Western European Continental Shelf (Huthnance et al., 2009). All these studies illustrate the complexity and key role of this transition region between coastal and open oceans.

The Bay of Biscay (Figure 1) is one of the key constituents of the Western European Continental Shelf in the North Atlantic, playing an important role in the interactions between the continental shelf and the open ocean waters. Narrow in its southern part (~30 km), this continental shelf gradually becomes wider northward, reaching ~180 km off Brittany (Charria et al., 2013). Together with internal tides and Ekman flow, these changes in shelf width strongly influences the continental slope current (Pingree and Garcia-Soto, 2014). The slope current has been identified as a seasonally varying current (Pingree and Le Cann, 1990), with a seasonal reversal of direction, northward in winter and southward in summer (Charria et al., 2013, Porter et al., 2016). In the Northeast Atlantic, the interannual variability of the slope current (maximum poleward flow in winter and equatorward in summer) varies with region, extending from the Iberian shelf in the south to the Shetland shelf in the north (Xu et al., 2015). The seasonal difference in current intensity deduced from altimetry reaches ~8-10 cm s^{-1} in the northern region of the Northeast Atlantic, but is limited to ~5 cm s^{-1} on the Bay of Biscay slopes. Instabilities in the slope current may lead to the generation of coherent mesoscale structures (Charria et al., 2017), such as the slope water oceanic eddies (SWODDIES) (Pingree and Le Cann 1992a; Pingree and Le Cann 1992b; Garcia-Soto et al., 2002; Caballero et al., 2014, Rubio et al., 2018, Manso-Narvarte et al., 2018). Slope current instabilities and associated eddy generation have been documented in different studies with a focus on the southeastern Bay of Biscay (Caballero et al., 2014, Rubio et al., 2018). However, eddy activity in the northern part of the bay remains unclear because only a very few studies based on drifter data have been carried out (Van Aken, 2002; Charria et al., 2013). In the northern part of the bay, the eddy generation mechanism is related to the influence of topographic features and the instability of

the slope current. However, another mechanism , namely front activity , may be contributing to eddy generation (Badin et al., 2009). The northern (north of 45^{o}N) part of the Bay of Biscay displays fully developed frontal activity (Yelekçi et al., 2017) and these fronts (particularly tidal fronts) may foster eddy activity.

Although the circulation and hydrography in the Bay of Biscay have been widely documented, knowledge on the processes driving cross-shelf exchanges in the region is limited to suggestions of cross-shelf flows following drifter trajectories (Porter et al., 2016) and modelling studies documenting cross-shelf flow events of fresh shelf waters (Reverdin et al., 2013). In a recent study, Rubio et al. (2018) showed the eddy-induced cross-shelf export of high chlorophyll-*a* waters in the southeast Bay of Biscay. Although these studies provide a perspective on cross-shelf transport mechanisms, there are only rough quantitative estimates of cross-shelf exchanges (Huthnance et al., 2002, 2009).

The present study details various processes leading to cross-shelf exchanges and quantifies the cross-shelf volume transports.

Description of data, model and methods is given in Section 2. Main results are detailed in Section 3. Section 3.1 describes along-shelf and cross-shelf circulation. Section 3.2 focuses on temporal and spatial distributions of cross-shelf exchanges. Impacts of mesoscale activity are presented in Section 3.3. The wind contribution to cross-shelf exchanges is given in Section 3.4. Discussion is presented in Section 4. Finally, Section 5 presents the conclusion.

2. Methodology

Identification and investigation of cross-shelf exchanges remains a challenge due to the complex nature of the processes involved, thus requiring a holistic approach. We thus used remotely sensed sea-surface temperatures and chlorophyll-*a* concentrations and high-resolution numerical simulations for exploration. In addition, we applied an eddy-detection and -tracking algorithm to simulated geostrophic velocity fields to study the cross-shelf exchanges in the Bay of Biscay.

The remotely sensed sea-surface temperature data used in this study were the daily nighttime Level 2 ungridded products with ~1 km resolution available from a moderate resolution imaging spectroradiometer (MODIS) sensor on Aqua and Terra satellites from 2007 to 2010. Data were downloaded from the Physical Oceanography Distributed Active Archive Center (PO.DAAC, https://podaac.jpl.nasa.gov/) operated by NASA. The dataset for the Bay of Biscay had been previously extracted and analyzed to explore the frontal dynamics in the region (Yelekçi et al., 2017).

Remotely sensed chlorophyll-*a* concentrations with ~1 km resolution for the North Atlantic Ocean were collected through the EU Copernicus Marine Environment Monitoring Service (marine.copernicus.eu) for the 2007-2010 period. This product estimates chlorophyll-*a* concentrations using the OC5CI algorithm, a combination of OCI (Hu et al., 2012) and OC5 (Gohin et al., 2008), using OCI for open/case-1 waters and OC5 for coastal/case-2 waters.

Simulations from two different configurations of the MARS3D model (Lazure and Dumas, 2008) were used for this study. The first configuration had been developed as part of the coastal

operational oceanography project PREVIMER (Dumas et al., 2014, http://www.previmer.org and http://marc.ifremer.fr/en for recent simulations), running operationally (2006-ongoing), with 2.5 km horizontal resolution, 40 sigma levels with hourly outputs. Open boundary conditions were extracted from PSY2V4 Mercator-Ocean simulations (http://mercator-ocean.fr). Atmospheric forcings were taken from the Meteo-France ARPEGE high-resolution and AROME models. For details on the PREVIMER configuration, see Yelekçi et al. (2017) and references therein.

The second MARS3D model simulation used in this study was based on the BACH1000 configuration (Theetten et al., 2017). The analyzed simulation is a hindcast (2001-2010) with 1 km horizontal resolution, 40 sigma levels and daily outputs. Open boundary conditions were extracted from the DRAKKAR NEMO global simulations with 1/12^{o} spatial resolution and the atmospheric forcings were based on the global atmospheric reanalysis ERA-Interim produced by the European Centre for Medium-Range Weather Forecasts (ECMWF). Bathymetry used here (Figure 1) is a composite of several IFREMER digital terrain models (DTMs) with 100 m resolution along the coast covering the French part of the continental shelf supplemented with a 1 km resolution DTM covering the Bay of Biscay and with a 1 nautical mile resolution from the North West Shelf Operational Oceanographic System (http: //noos.bsh.de). Both DTMs and the mean sea level were interpolated on the grid and merged. More details on the BACH1000 configuration and the validation of the simulations can be found in Charria et al. (2017) and Theetten et al. (2017).

Outputs of these two configurations were compared with the remotely sensed products. Although both configurations were able to simulate features with a length scale larger than 20 km (related with the effective resolution ~ 7 times the model spatial resolution - Marchesiello et al., 2009), the PREVIMER configuration was not able to simulate smaller scale features that

constitute a considerable amount of the observed (sub)mesoscale activity (seen on remotely sensed sea-surface temperature and chlorophyll-*a* images) over the shelf break. Therefore, in this study, we present the results from the BACH1000 simulations only.

In this study, we investigated 2007-2010 for cross-shelf exchanges. There are two main reasons for selecting this 2007-2010 period. First, both models, as well as satellite data, are available for this period. Second, and importantly, the number and quality of *in situ* observations were higher during this period, allowing better validation of the numerical models used. Since 2007, a fishery observation network (RECOPESCA, Leblond et al., 2010; Lamouroux et al.,2016) has been setup, providing additional profiles, particularly over the shelf and the shelf break. During 2009-2010, ASPEX experiments (deployment of 12 ADCP during 2 years – Le Boyer et al., 2013; Kersalé et al., 2016) provide a unique dataset to validate model simulations during this period.

The study area is the northern part of the Bay of Biscay, area bounded by 45^{o}N-49^{o}N and 1^{o}W-12^{o}W. For this area, satellite images of sea-surface temperatures and chlorophyll-*a* were carefully screened for eddies and filaments over the shelf break. Numerous features were detected. Model results (both configurations) were investigated and compared with the features observed through remotely sensed observations. BACH1000 simulations were able to successfully simulate different types of shelf-break eddies and filaments. Observed features were further investigated using the model outputs, to explore the mechanism behind the formation/dissipation of the features and their impact on cross-shelf exchanges.

Fluxes across the shelf and deep regions were estimated along an enclosed boundary (red line in Figure 1), approximating the 500 m isobath on the model grid. At each time step and depth, velocity vectors were projected orthogonal to the 500 m isobath to obtain the cross-shelf fluxes.

Daily upslope (downslope) transports were calculated by integrating upslope (downslope) fluxes horizontally across each grid point on the 500 m isobath and vertically from the surface to the bottom (Equations 1a, 1b). Daily net transport was obtained by summing the daily upslope and downslope transports (Equation 1c).

$$\text{(1a)} \quad VT_{z1,z2}^{upslope} = \int_{start}^{end}\int_{z1}^{z2}(U\,.\,\vec{n})\,dz\,dl \qquad \text{if} \qquad U\,.\vec{n} < 0$$

$$\text{(1b)} \quad VT_{z1,z2}^{downslope} = \int_{start}^{end}\int_{z1}^{z2}(U\,.\,\vec{n})\,dz\,dl \qquad \text{if} \qquad U\,.\vec{n} > 0$$

$$\text{(1c)} \quad VT_{z1,z2}^{NET} = VT_{z1,z2}^{upslope} + VT_{z1,z2}^{downslope}$$

Where $VT_{z1,z2}^{upslope}$ and $VT_{z1,z2}^{downslope}$ represent the upslope and downslope volume transports, respectively, at time step t. They are integrated between depths z1 and z2, and the start and end points of the boundary (500 m isobath). U=U(t,z,l) is the horizontal velocity vector on the boundary and $\vec{n}$ is the unit vector pointing downslope and normal to the boundary, z denotes depth and l is the length of the boundary (500 m isobath). Positive values represent downslope transport and negative values upslope transport (see arrows in Figure 1). The sum of downslope and upslope volume transports denote the net volume transport. Hereafter, we refer to "net volume transport" to interpret cross-shelf exchanges, and "upslope" or "downslope" represent the direction of the net volume transport. The "flux" term is used to represent fluxes (*i.e.* transport per unit area), as in Figures 4 and 5.

To obtain an overview of eddy activity, as well as to observe their spatio-temporal variability, we applied an eddy-detection and -tracking algorithm. To do so, we used the angular momentum eddy-detection and -tracking algorithm (AMEDA - Le Vu et al., 2018). Although there are numerous algorithms available for such purposes, we preferred this method because it employs minimal number of tunable parameters and it is robust to the grid resolution (Le Vu et al.,2018).

AMEDA was applied to the modelled velocities to obtain the eddy census, as well as their physical properties. AMEDA detects eddy centers as the maximum of the local normalized

angular momentum (LNAM), as proposed in Mkhinini et al. (2014). The objective is to compute an integral value of the angular momentum in a limited area, which will be maximum at the eddy center (Le Vu et al., 2018). Considering this parameter alone is not sufficient to define an eddy, a second criterion is needed. Similar to other algorithms (Chaigneau et al., 2009; Nencioli et al., 2010), AMEDA uses a geometric criterion. Thus, eddy centers detected by LNAM maxima are kept only if they have a closed streamline around them. Characteristic contours associated with the eddy are defined using the size and velocity of the closed streamlines surrounding the eddy center. First, all closed streamlines were identified. Then, for each one, the mean radius was calculated, which is equal to the radius of a circle with the same area as that defined by the closed streamline. Second, the mean velocity was calculated from the circulation along the closed streamline. Finally, the streamline corresponding to the highest mean velocity was used to define the characteristic contours of the eddy.

To connect this local tracking methodology to cross-shelf transports, a filtered dataset of BACH1000 model simulations was created. Based on the convolution of the modelled fields with a Hanning window (with a window size of 50 km), each modelled field (current velocities, temperature and salinity for each vertical layer and time step) was filtered to obtain large-scale (larger than 50 km) circulation. The difference between filtered and unfiltered simulations can then be considered as the mesoscale dynamics (called “eddy-induced” circulation).

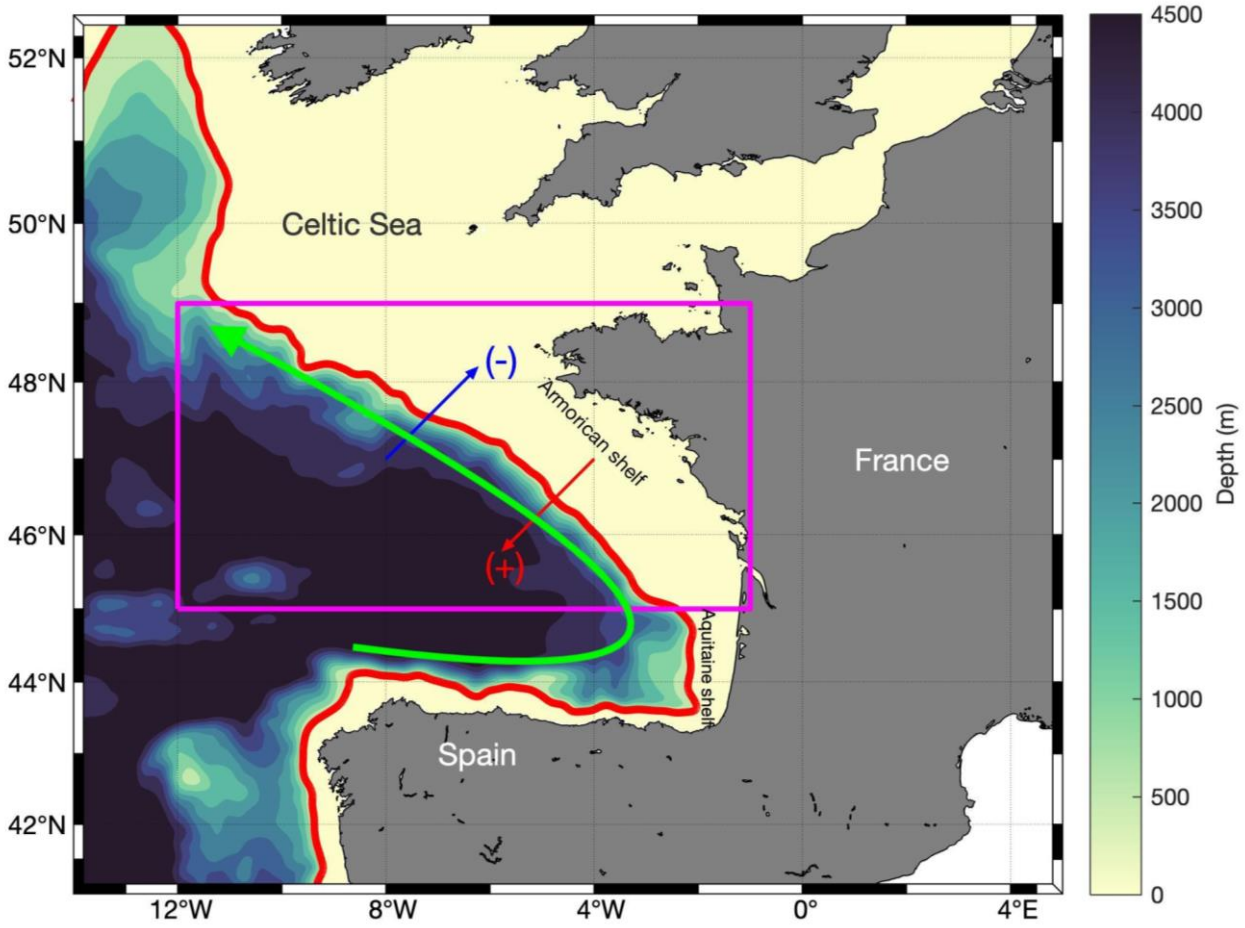

Figure 1. Bathymetry of the region (from Ifremer digital terrain models with 100 m to 1 km merged with the North West Shelf Operational Oceanographic System - http://noos.bsh.de). The magenta boxed area represents the study domain bounded by 45°N-49°N and 12°W-1°W. The red line represents the 500 m isobath, which is used for integrating the cross-shelf transport. Downslope (upslope) transport direction is denoted by plus (minus) sign. Green arrow represents the slope current direction in winter.

3. Results

To detail cross-shelf exchanges in the northern Bay of Biscay, results were divided into four sections. The first section introduces our simulated along-shelf and cross-shelf currents to give an overview of slope circulation. In the second section, the variability of the cross-shelf Eulerian transports is detailed. In the third and fourth sections, the roles of mesoscale activity and wind forcing, respectively, are presented.

3.1 Along-shelf and cross-shelf circulation

The continental slope ocean circulation is generally described through its dominant along-shelf component. Although the present study focuses on cross-slope exchanges, it is important to emphasize the relative magnitudes of along-shelf and cross-shelf currents.

At the surface, cross-shelf currents had similar magnitudes as those of along-shelf currents, or even became (locally) stronger for short time periods (Figure 2a). However, spatially averaged mean currents at the shelf break (500 m isobath) showed that along-shelf currents are stronger than cross-shelf currents over time (Figure 2a-c). At 200 m depth, the along-shelf average currents can exceed 0.1 m s^{-1}. On the other hand, cross-shelf current velocities were around 0.02 m s^{-1} at those intermediate depths. Deeper, close to the bottom, around 400 m depth, the dominance of along-shelf circulation was confirmed with along-slope currents 3 to 5 times larger than the cross-shelf component. Concerning the along-shore currents, they present similar magnitudes when they flow poleward or equatorward.

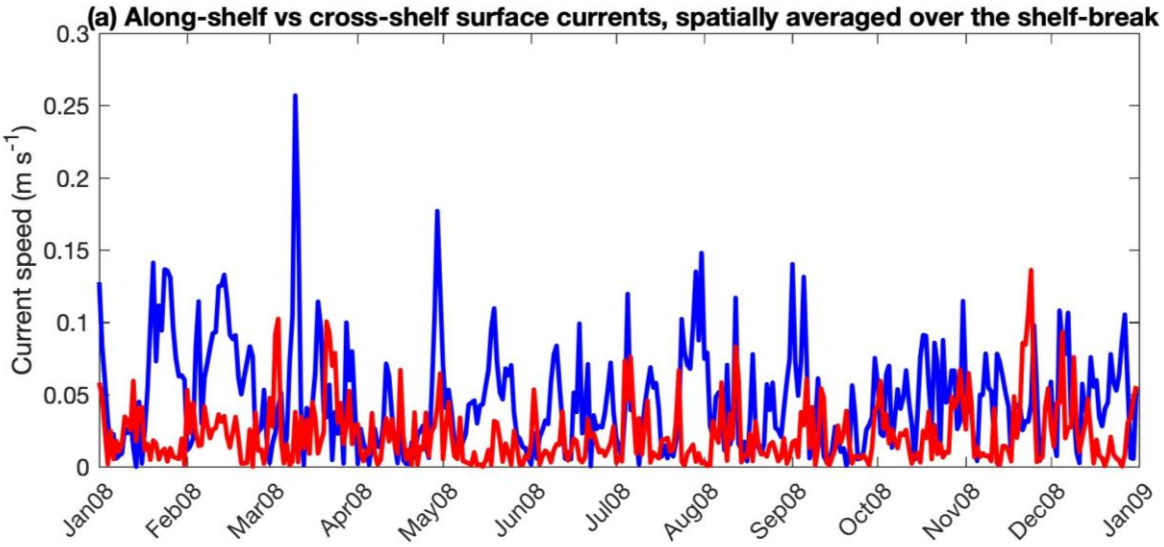
(a) Along-shelf vs cross-shelf surface currents, spatially averaged over the shelf-break
Current speed (m s-1)
0.3
0.25
0.2
0.15
0.1
0.05
0
Jan08
Feb08
Mar08
Apr08
May08
Jun08
Jul08
Aug08
Sep08
Oct08
Nov08
Dec08
Jan09

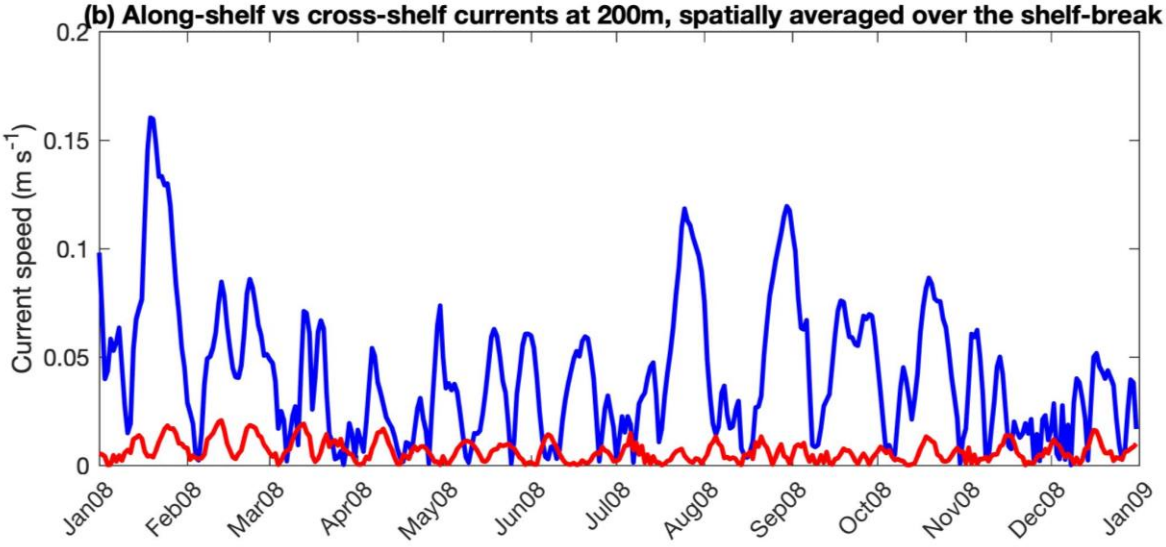
(b) Along-shelf vs cross-shelf currents at 200m, spatially averaged over the shelf-break
Current speed (m s-1)
0.2
0.15
0.1
0.05
0
Jan08
Feb08
Mar08
Apr08
May08
Jun08
Jul08
Aug08
Sep08
Oct08
Nov08
Dec08
Jan09

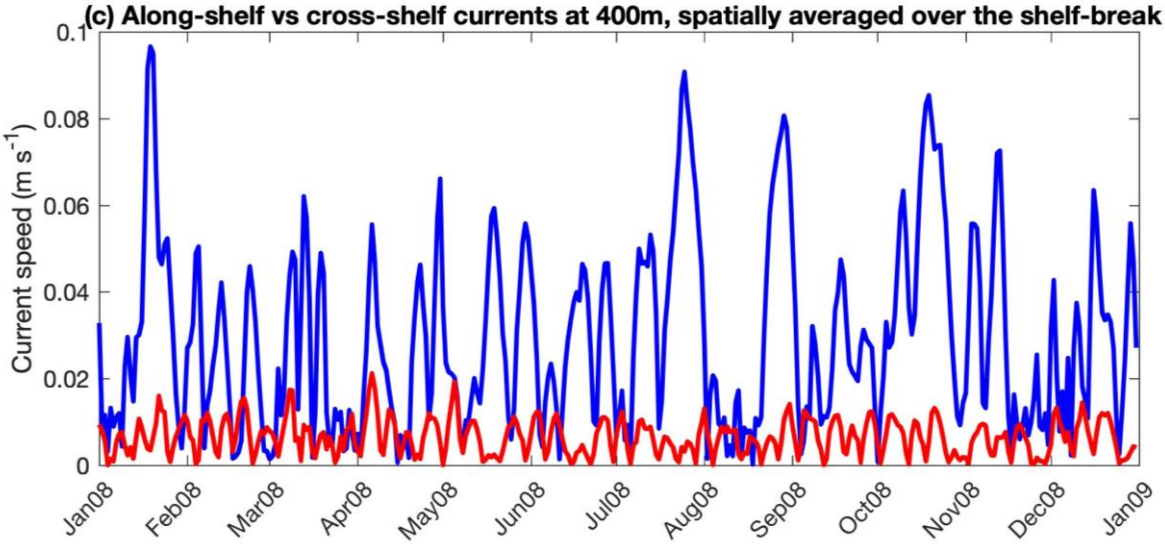
(c) Along-shelf vs cross-shelf currents at 400m, spatially averaged over the shelf-break
Current speed (m s-1)
0.1
0.08
0.06
0.04
0.02
0
Jan08
Feb08
Mar08
Apr08
May08
Jun08
Jul08
Aug08
Sep08
Oct08
Nov08
Dec08
Jan09

283

Figure 2. Along-shelf (blue) and cross-shelf (red) currents (m s^{-1}) at the shelf break in 2008: (a) at the surface, (b) at 200 m and (c) at 400 m depth. Currents are spatially averaged along the 500 m isobath for each date.

Despite similar amplitudes at the surface and at mid-depths, along-shelf currents were generally stronger than cross-shelf currents (Figure 2b). Modelled fields show that at mid-depths (200-350 m) cross-shelf currents can occasionally become dominant. However, the number of these situations is very limited.

3.2 Spatial and temporal evolution of cross-shelf transports

The time-series of vertically integrated volume transports across the shelf break during 2007-2010 shows a fluctuating pattern (Figure 3). The signal related to these fluctuations was analyzed using a spectral Fourier analysis (not shown). The energy spectrum exhibited peaks at 14-day and 28-day periods, which represent the imprint of lunar fortnightly and lunar monthly tidal components, respectively. To evaluate the residual transport, time-series were smoothed (31-day moving average; Figure 3, red line) to filter short-term oscillations (mainly tidal components).

The general direction of the transport was upslope. Upslope transport was 1.75±1.1 Sv on average. Larger volumes of upslope transport were generally observed during winter, with maximum values exceeding 6 Sv. Average value of downslope transport was 1.17±0.9 Sv. Strong upslope transports were modelled on January-February 2008, 2009 and 2010. The peak upslope transport was observed in winter 2010 with 6.9 Sv, whereas the downslope transport maxima was observed in late autumn 2007 with -8.4 Sv. Cumulative mean transports for each

year are given in Table 1. Yearly mean downslope transports ranged between 3.62±0.95 Sv and 3.81±1.05 Sv and mean upslope transports ranged between 4.29±1.30 Sv and 4.74±1.54 Sv. All four years had a mean net transport in the upslope direction. Average net transport reached its maximum with -0.93 Sv in 2010 and minimum in 2009 with -0.55 Sv.

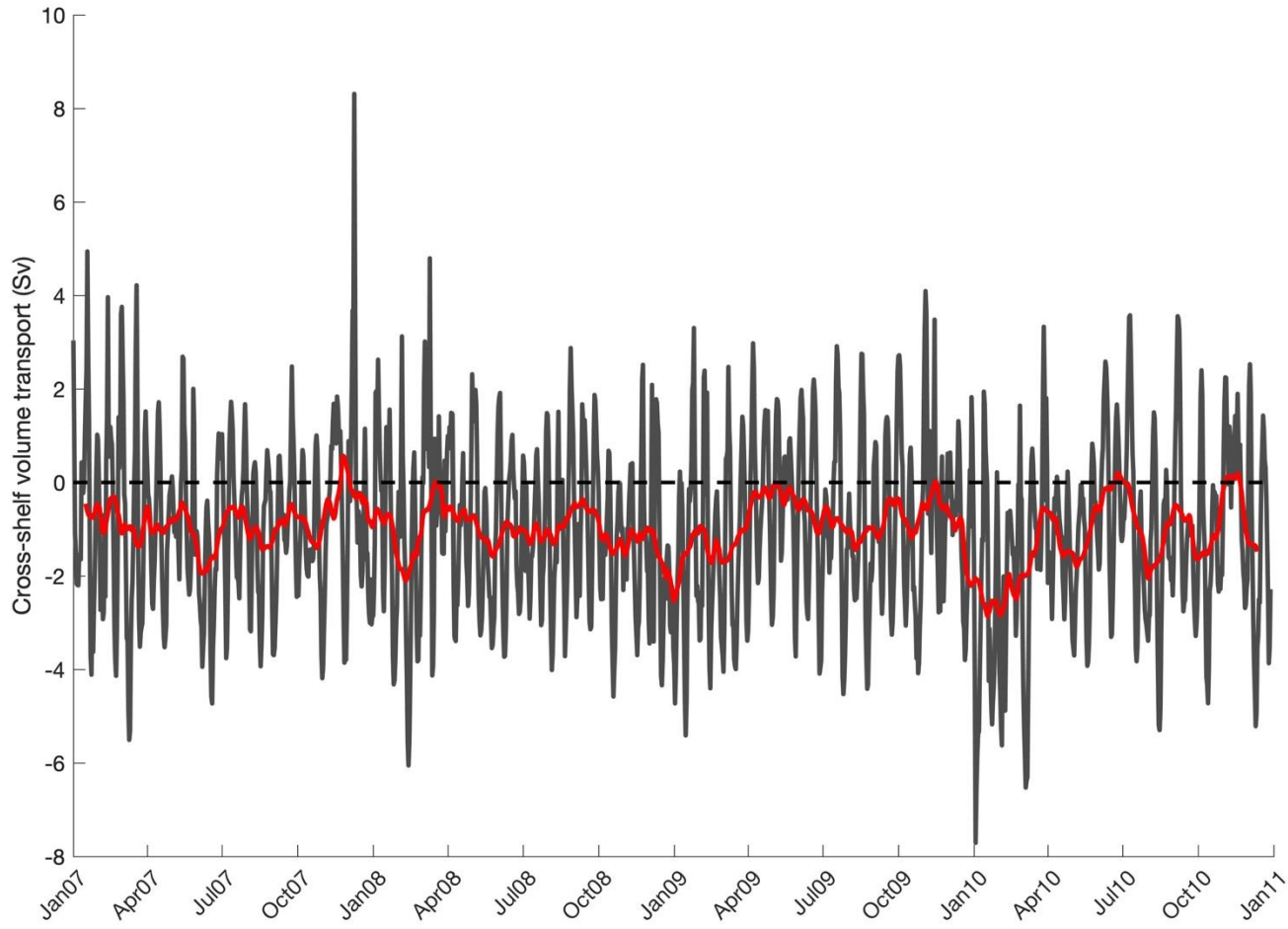

Figure 3. Distribution of vertically integrated daily volume transport (in Sv) across the 500 m shelf-break contour. Red line shows the smoothed time series (31-day window smoothing applied).

Table 1. Mean volume transport (Surface-500 m) through shelf break in 2007-2010. Positive values represent downslope transport (in Sv).

Year	Cumulative mean downslope transport	Cumulative mean upslope transport	Cumulative mean net transport
2007	3.69±1.09	-4.32±1.35	-0.63
2008	3.62±0.95	-4.37±1.18	-0.75
2009	3.74±0.88	-4.29±1.30	-0.55
2010	3.81±1.05	-4.74±1.54	-0.93

Surface (upper 50 m) and subsurface (mid-layer) transports predominantly had opposite directions (Figure 4). These short-lived and mostly local events, were generally associated with intense transports at the surface (Figure 4). These features are not visible in the annual evolution of volume transports (expressed as fluxes, i.e. transport per unit area; Figure 5), because they are short-lived events with a relatively minor contribution to the overall picture. The dominant feature observed in annual distributions of volume flux was a change of sign around 350-400m between 47-48^{o}N. The depth of this transition changed in space and time, but positive values in the bottom boundary layer remain clearly visible in all (2007-2010) annual mean volume flux distributions (only 2008 is shown, Figure 5).

Upslope (negative) transport with a core around 250-300 m was observed (Figure 5), with a maximum value of 0.25 $m^3\ s^{-1}\ m^{-2}$ and a mean value of 0.05 $m^3\ s^{-1}\ m^{-2}$ (annual mean). Bounded by this layer and the bottom boundary layer, a downslope (positive) flux with a maximum value of 0.20 $m^3\ s^{-1}\ m^{-2}$ and a mean value of 0.05±0.01 $m^3\ s^{-1}\ m^{-2}$ (annual mean) was modelled.

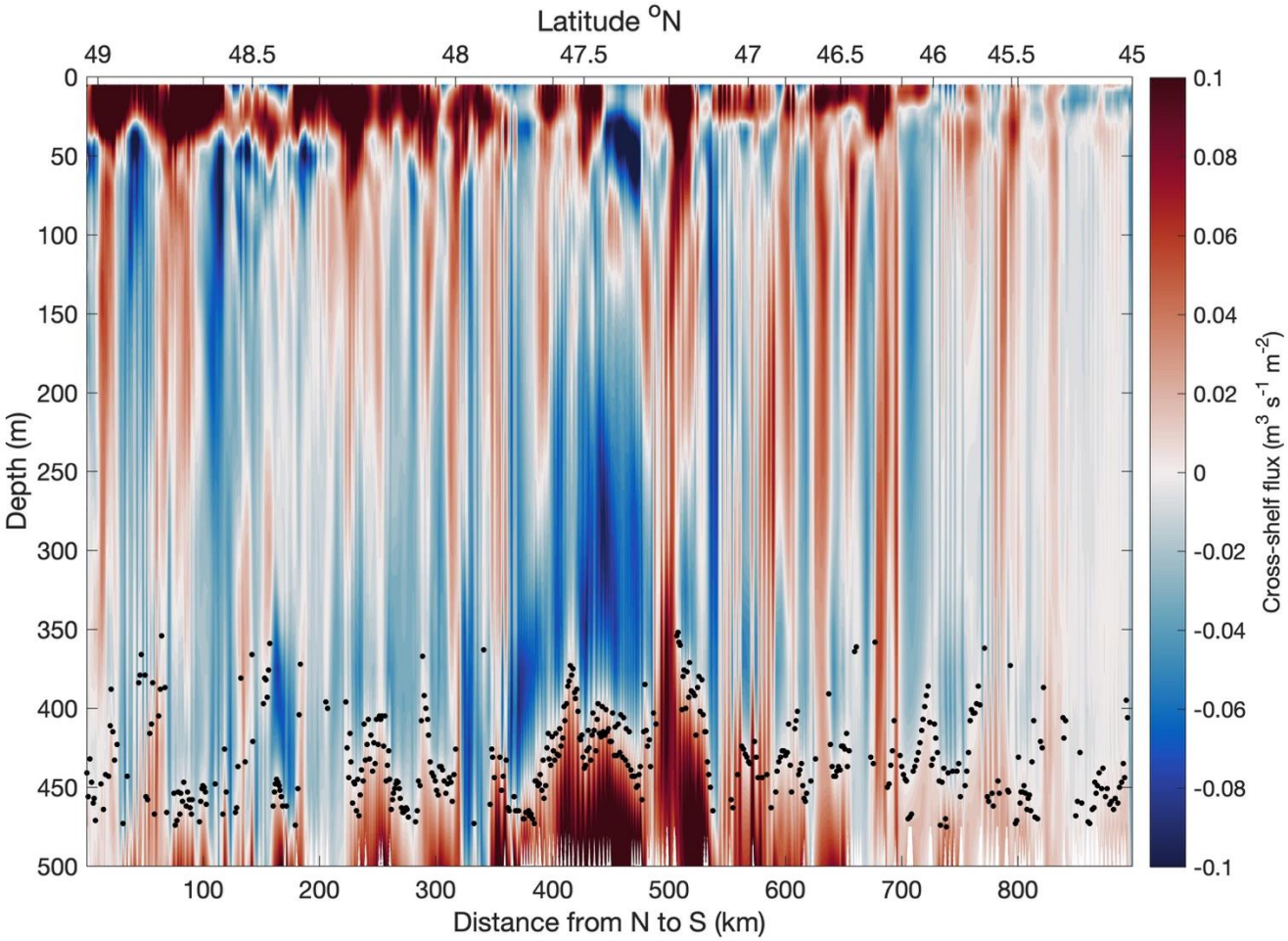

Figure 4. Vertical section of cross-shelf fluxes ($m^3\ s^{-1}\ m^{-2}$) along the 500 m isobath on 5 July 2008. Black dots represent the estimated bottom boundary layer.

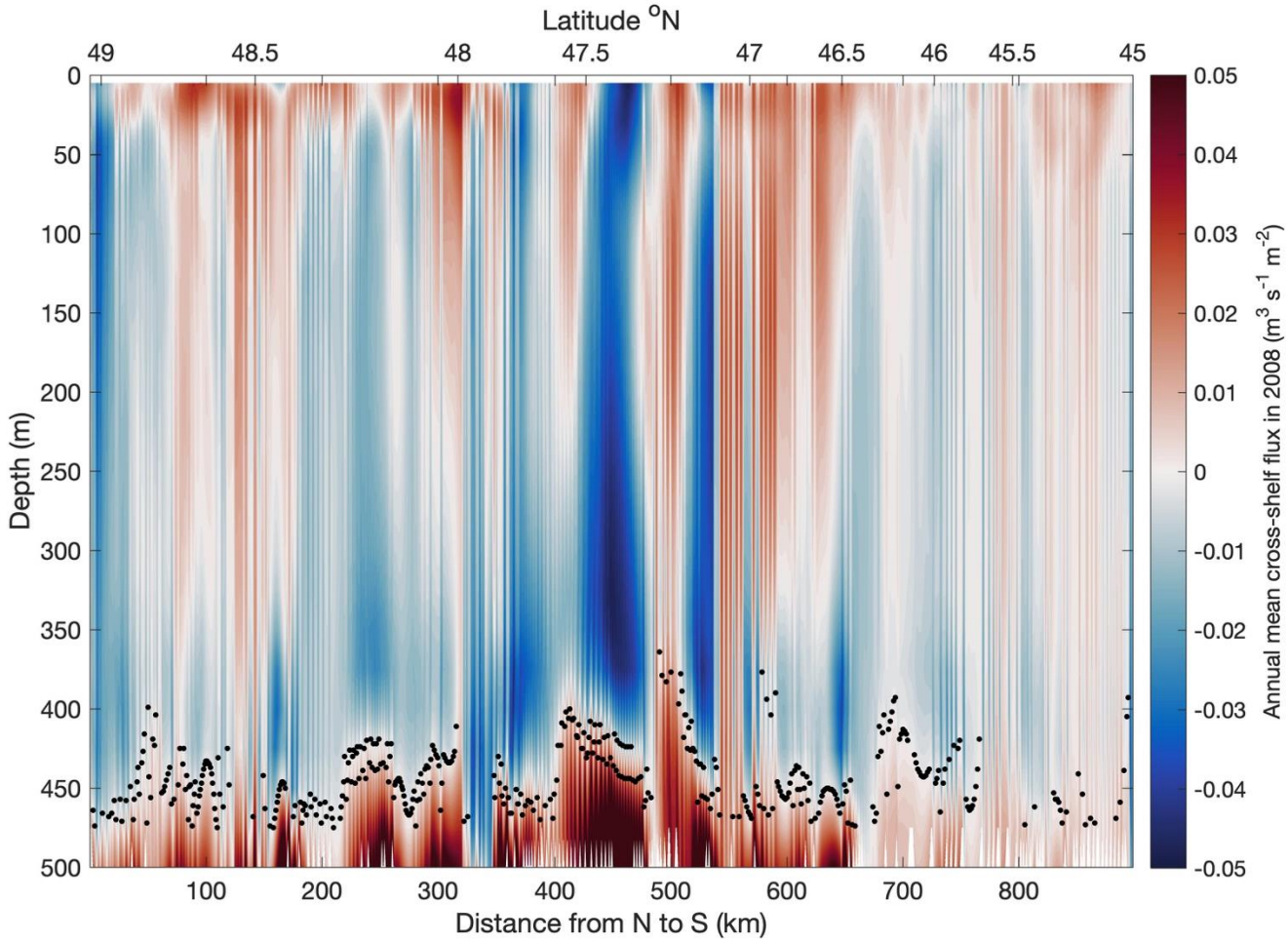

Figure 5. Vertical section of annual mean cross-shelf fluxes ($m^3\ s^{-1}\ m^{-2}$) along the 500 m isobath in 2008. Black dots represent the estimated bottom boundary layer.

Volume fluxes displayed vertical variability along the shelf break visible on daily snapshots (Figure 4) and also annual means (Figure 5). The clear vertical layers observed in daily averages were as follows: a surface transport pattern, a subsurface transport pattern, occasionally in the opposite direction (until the bottom boundary layer), and finally another pattern in the bottom boundary layer.

353 Regardless the direction of the flow at the surface, this bottom boundary flow was almost
354 always oriented downslope. This bottom boundary flow was a ubiquitous feature appearing
355 throughout the study time period, and also present in the annual mean transport scheme (Figure
356 5).
357 Along the 500 m contour, this bottom boundary flow is both stronger and thicker between 47°N
358 and 48°N, corresponding to Chapel Bank. In this region, flux values were typically around 0.1
359 $m^3 s^{-1} m^{-2}$ and reached maximum values of around 0.2 $m^3 s^{-1} m^{-2}$. The thickness of this bottom
360 downslope flow varied spatially along the 500 m contour. The upper boundary of this layer was
361 typically around 400 m. Bottom transport estimates (integrated between 400 m and 500 m) had
362 a mean transport (in 2007-2010) of 0.9±0.6 Sv, occasionally reaching a maximum of 2.5 Sv.
363 Here, we define the bottom boundary layer as the parcel of water bounded by the ocean floor
364 and the depth at which velocity changes sign (black dots in Figure 5). With this dynamic
365 definition, we obtained the dynamic bottom boundary layer thickness (Figure 6) and associated
366 volume transports. In this layer, we estimated a mean volume transport (2007-2010) of 0.76±0.4
367 Sv. Based on the dynamic definition, we obtained a mean (2007-2010) bottom boundary
368 thickness of 65±6 m, which is slightly less than our initial assumption of 100 m (fixed thickness
369 between 400 m and 500 m). Spectral Fourier analyses of bottom boundary flow time series (not
370 shown) gave peaks at 14 and 28 days.

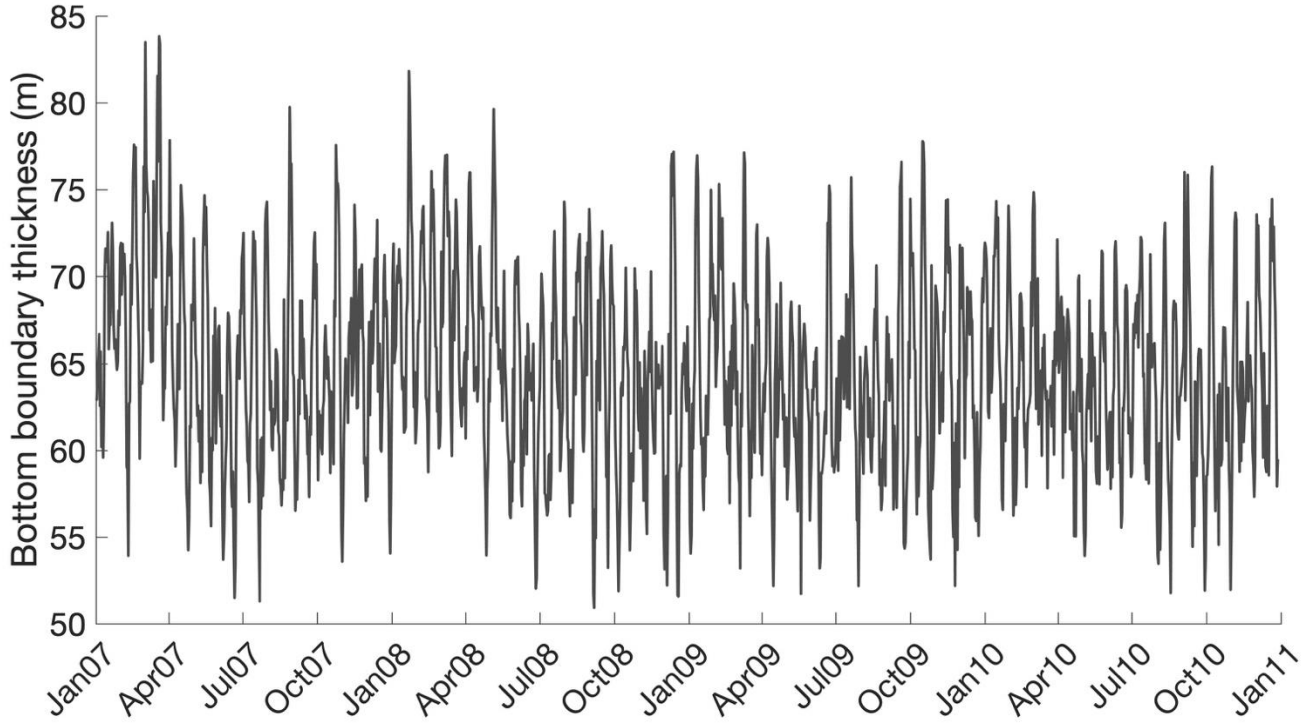

Figure 6 Temporal evolution of the bottom boundary layer thickness. Bottom boundary layer is defined simply as the deepest point in the water column where the flow changes sign. Figure shows the mean thickness along the 500 m isobath for each time step.

Persistent bottom boundary thickness and downslope transport observed around the 500 m contour was not observed at 1000 m. At the 1000 m contour, the bottom boundary thickness (not shown) was highly variable. Bottom boundary layer could not be observed persistently and its thickness occasionally exceeded 200 m. Although a maximum was observed between 47^{o}N and 48^{o}N, similar to the 500 m contour, the signature was less pronounced than the pattern observed around the 500 m contour. Also, the bottom boundary flow observed at the 1000 m contour was weak compared with the flow observed at the 500 m depth contour. The typical flow was less than 0.05 m s^{-1}.

This bottom boundary flow represents an important component of the cross-shelf exchanges, because this circulation was simulated over the whole year (not shown) with a magnitude

comparable to the surface boundary exchange at the 500 m contour. The largest magnitudes were observed between the 400 m and 600 m contours. Magnitude of this near-bottom flow gradually decreased towards the open ocean, reaching a minimum at the 1000 m contour.

3.3 Mesoscale activity and cross-shelf exchanges

To understand the possible impact of shelf-break eddies on cross-shelf exchanges, we first considered a wider perspective. Using the AMEDA eddy-tracking algorithm (Le Vu et al., 2018), we studied the evolution of shelf-break eddies and their links with cross-shelf transports over time. We were mainly interested in eddies near the shelf break; we therefore identified eddies whose centers lay between the 200 m and 2500 m isobaths (called "shelf-break eddies") and had a radius larger than 5 km. Following estimations from the eddy-tracking algorithm, the contribution of the detected eddies to cross-shelf transport was evaluated considering modelled filtered (i.e. filtering spatial features lower than 50 km) fields versus the total cross-shelf transport.

Although the number of shelf-break eddies was highly variable, the maximum (40) was observed in July-October (during the stratified period) and the minimum (5) in December-April (Figure 8). The eddy-tracking algorithm revealed that eddies have also larger size during the stratified period, typically around 20-30 km in the open ocean (deeper than 2500 m). Eddy presence, defined as the percentage of time (2007-2010) a grid point lies within an eddy, showed high and low eddy activity regions. Areas with eddy frequencies higher than 15% were mainly in the deep ocean (except few coastal areas), where large-size eddies were observed. The shelf break is another important area of eddy presence, reaching 13%. A specific feature

412 (Figure 7) was observed in an area (between 5ºW-7ºW and 46ºN-46.5ºN) with almost no eddy
413 presence (less than 5%) during the study period.
414

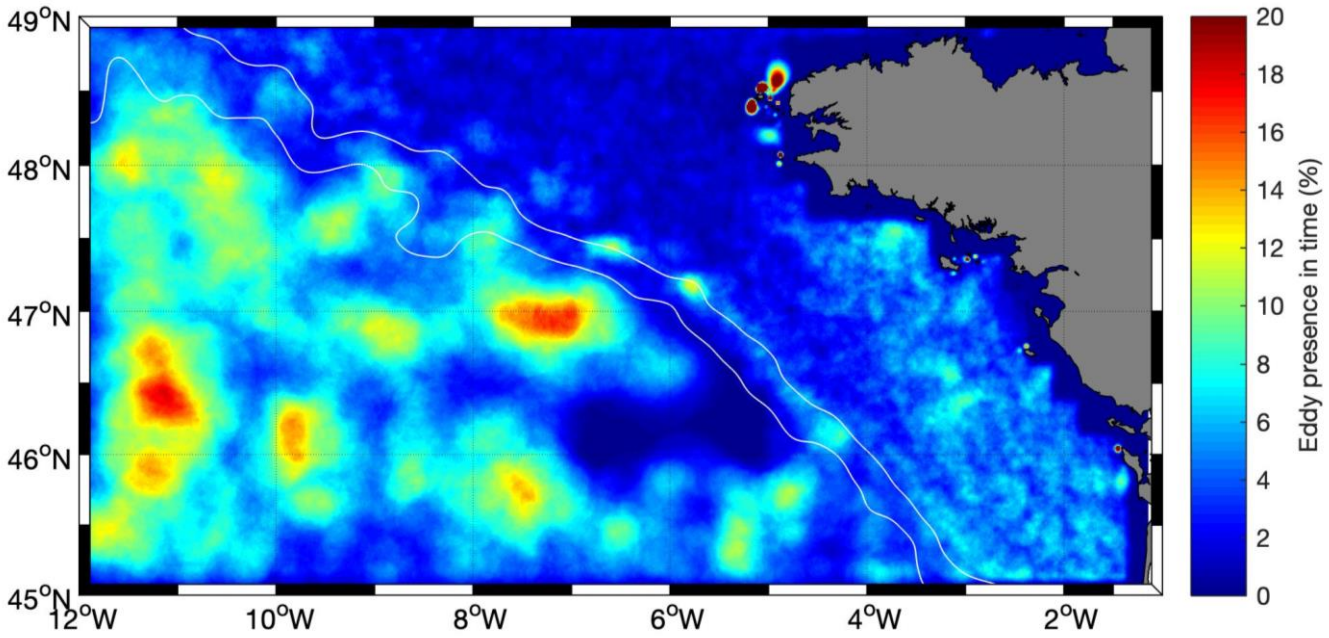

415

416 Figure 7. Eddy presence based on eddy-tracking algorithm results. Eddy presence is defined as
417 the percentage of time (during the 2007-2010 period) during which a grid point lies within an
418 eddy. White contours represent the 500 m and 2500 m isobaths.

419

420 Both eddy activity and cross-shelf transports are dynamic oscillating features. To gain a better
421 understanding of the relationship over time between transport and eddy activity, we examined
422 low-pass filtered time-series for both variables.
423 Figure 8 shows the low-pass filtered (31-day window) shelf-break eddy activity (number of
424 eddies between the 200 m and 2500 m isobaths) and the volume transport at the surface (0-50
425 m), along the 500 m isobath. As the number of eddies along the shelf break increased, upslope
426 (negative values) transport was observed at the surface. The number of eddies showed a
427 negative correlation (r=-0.55) with surface volume transport. The contribution of eddy activity

to the cross-shelf transports can be quantified by comparing modelled filtered fields (filtering out features smaller than 50 km) and the original unfiltered model simulations. The difference (Figure 9) was considered as the eddy-induced transport, knowing that dynamics of features smaller than 50 km were mainly related to eddy activity. For the layer at 0-50 m depth, the eddy-induced transport (Figure 10) was upslope (negative values) and contributed, on average over the study period, to 40% of the upslope transport (i.e. ratio between eddy-induced transport and total upslope transport). Eddies also represented a significant, albeit smaller, portion of the downslope transport (27% of the total transport). Then, in the surface layer, eddies tended to limit the export of shelf waters to the open ocean.

Transport at mid-depth layers (50-350 m) was mainly upslope (negative values) over time and was positively correlated (r=0.3) with the number of shelf-break surface-detected eddies. For this layer (50-350 m), the eddy-induced transport generally remained negative (upslope) (Figure 9), but the contribution of eddy-induced transport dropped to 33% of the total transport.

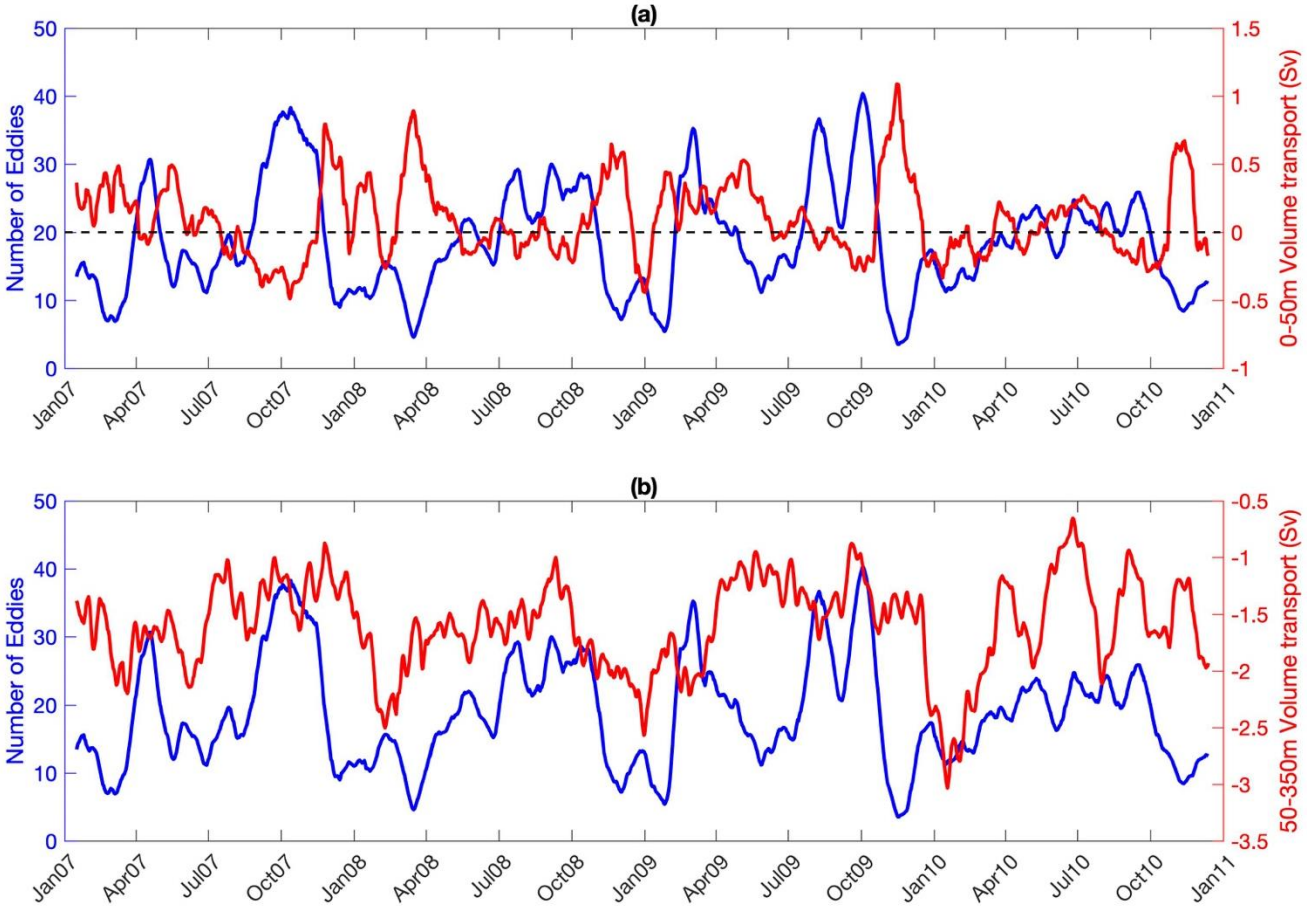

Figure 8. (a) Number of shelf-break eddies per day (blue) and 0-50 m volume transport (expressed in Sv; red) across the 500 m isobath. (b) Number of shelf-break eddies per day (blue) and 50-350 m volume transport (expressed in Sv; red) across the 500 m isobath. All variables were low-pass filtered using a moving window of 31 days.

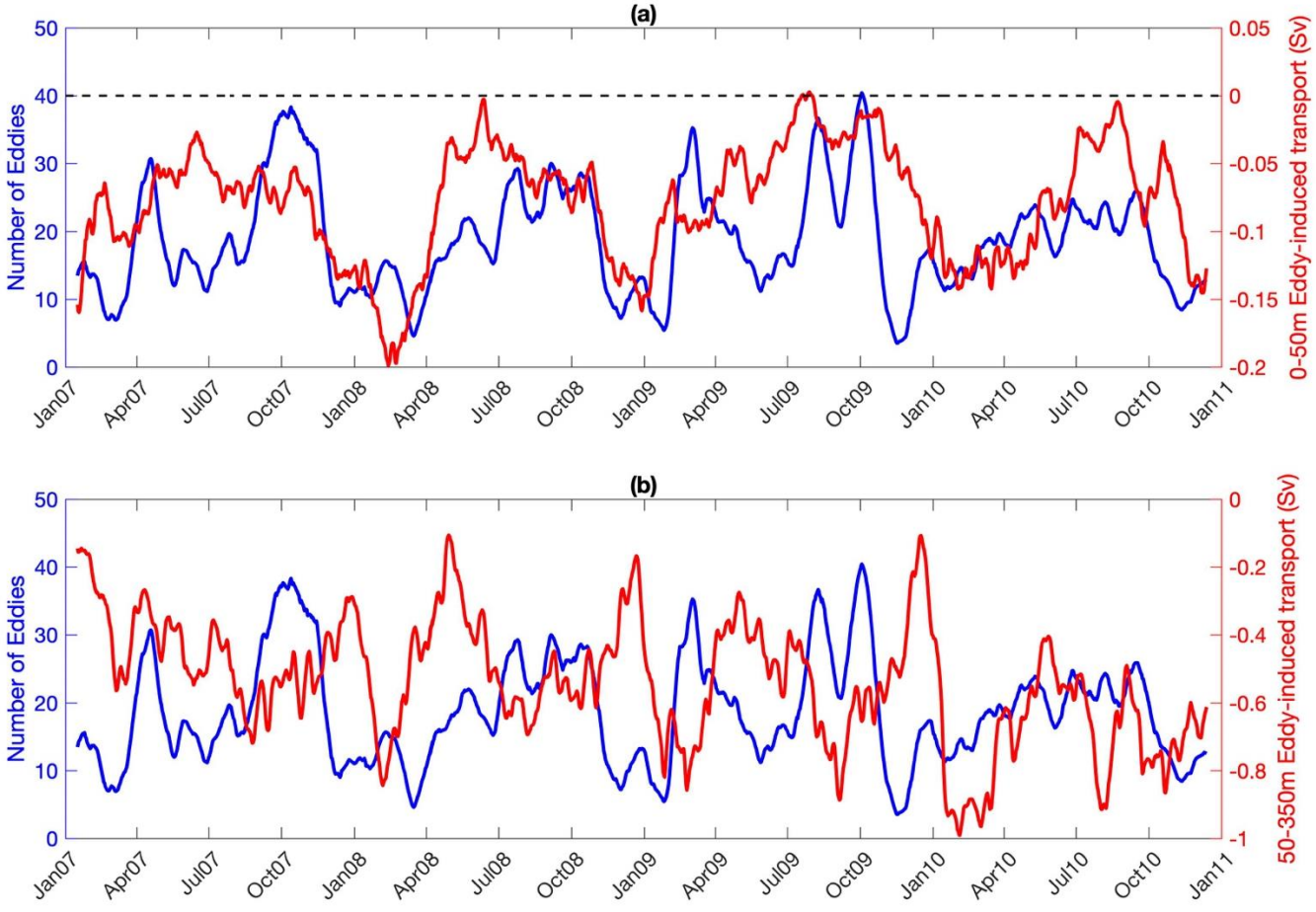

Figure 9. (a) Number of shelf-break eddies per day (blue) and 0-50 m eddy-induced transport (expressed in Sv; red) across the 500 m isobath. (b) Number of shelf-break eddies per day (blue) and 50-350 m eddy-induced transport (expressed in Sv; red) across the 500 m isobath. All variables were low-pass filtered using a moving window of 31 days.

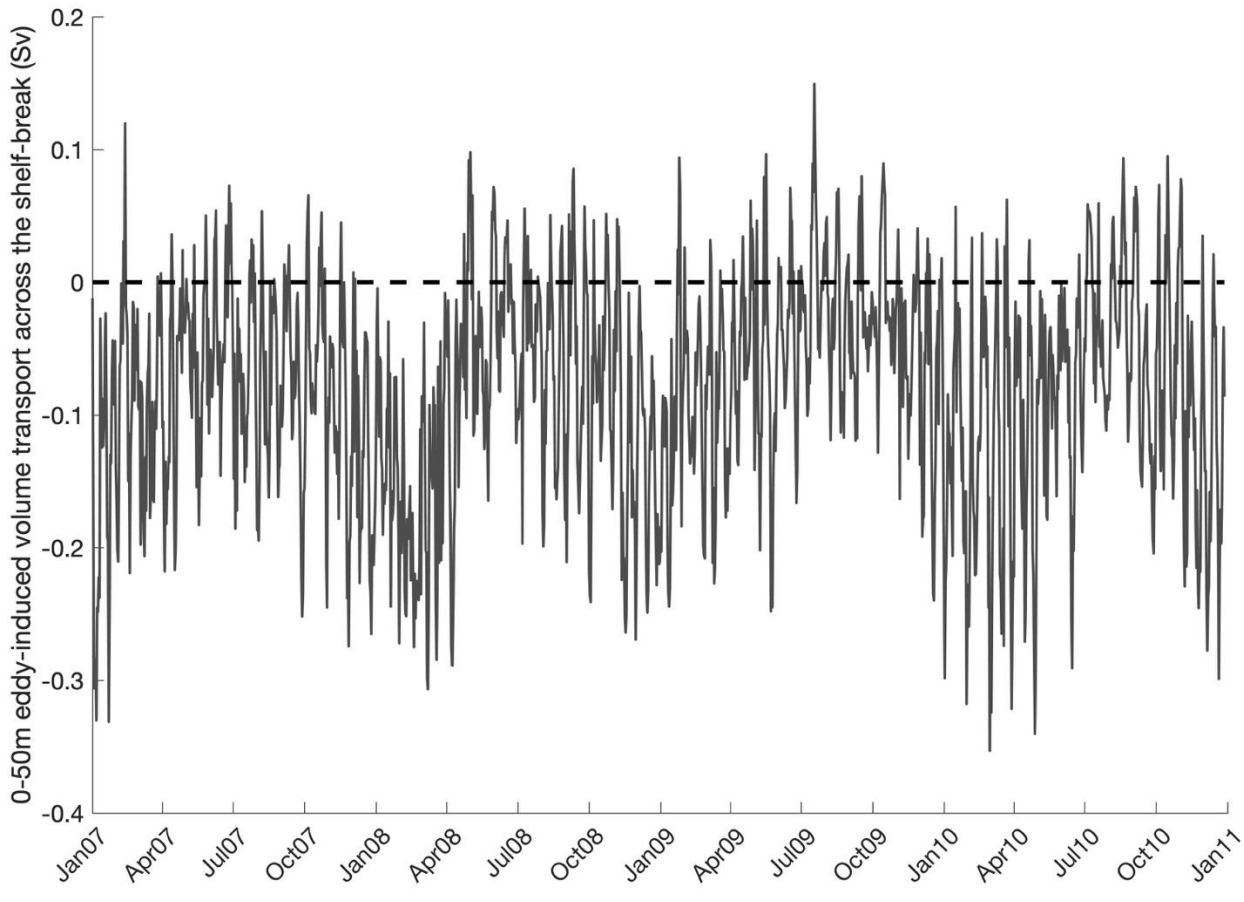

Figure 10. 0-50m eddy-induced volume transport (in Sv) across the 500m isobath.

Several examples of eddy-induced exchange events (exporting waters from the shelf to the open ocean) were identified, where individual eddies as well as eddy dipoles were observed. We detail one of these cases in May 2008: on 20 May, a cyclonic eddy was observed on satellite maps (with a pronounced signature in chlorophyll-a concentrations), centered on 46^{o}N, 4.5^{o}W (Figure 11). The eddy had a core temperature of ~15.5°C and colder (~14.5°C) waters on the periphery, carrying shelf-break waters downslope. Similar imprint of this eddy can be seen in the chlorophyll-a concentration, where the eddy had low concentrations (less than 0.4 mg m^{-3}) in its core and peripheral concentrations of 0.8 mg m^{-3}. Due to limited cloud-free satellite images, the exact lifetime of this eddy cannot be precisely estimated. Therefore, model outputs

were used to further investigate the formation, evolution and impact of this eddy on cross-shelf exchanges.

Although the turbulent nature of the simulated field did not always allow the reproduction of the exact time and/or location of the eddies, our simulations successfully reproduced the overall mesoscale activity with realistic eddies in terms of dimension and evolution. Furthermore, in some examples, the model closely reproduced the eddy field observed in consecutive satellite images.

Here, we present such an example where the model successfully reproduced the eddy and associated cross-shelf exchanges. According to our simulations and the information from the eddy-tracking algorithm, this eddy was born on 1 May at the shelf break, between the Saint-Nazaire Canyon (extending from 45.91^{o}N, 4.57^{o}W to 46.33^{o}N, 4.30^{o}W) and the Noirmoutier Canyon (extending from 45.87^{o}N, 4.44^{o}W to 46.04^{o}N, 4.05^{o}W), with a radius of 5 km, gradually increasing to a size of 27 km as it propagated downslope. The eddy had a lifetime of 71 days (disappearing on 13 July), with a mean radius of 15 km. Eddy distribution in the bay on 26 May is given in Figure 13.

In Figure 12 we show the simulated eddy for 26 May. As observed on the surface temperature and salinity distributions, the eddy transported colder and fresher waters downslope. A transect through the eddy center (45.8^{o}N) revealed stratification, with elevated isotherms within the eddy of interest. Thus, due to this cyclonic motion, shelf-break waters advected by the eddy were bound by the upper 250 m in its center. A typical azimuthal velocity of the eddy was ~20 cm s^{-1}.

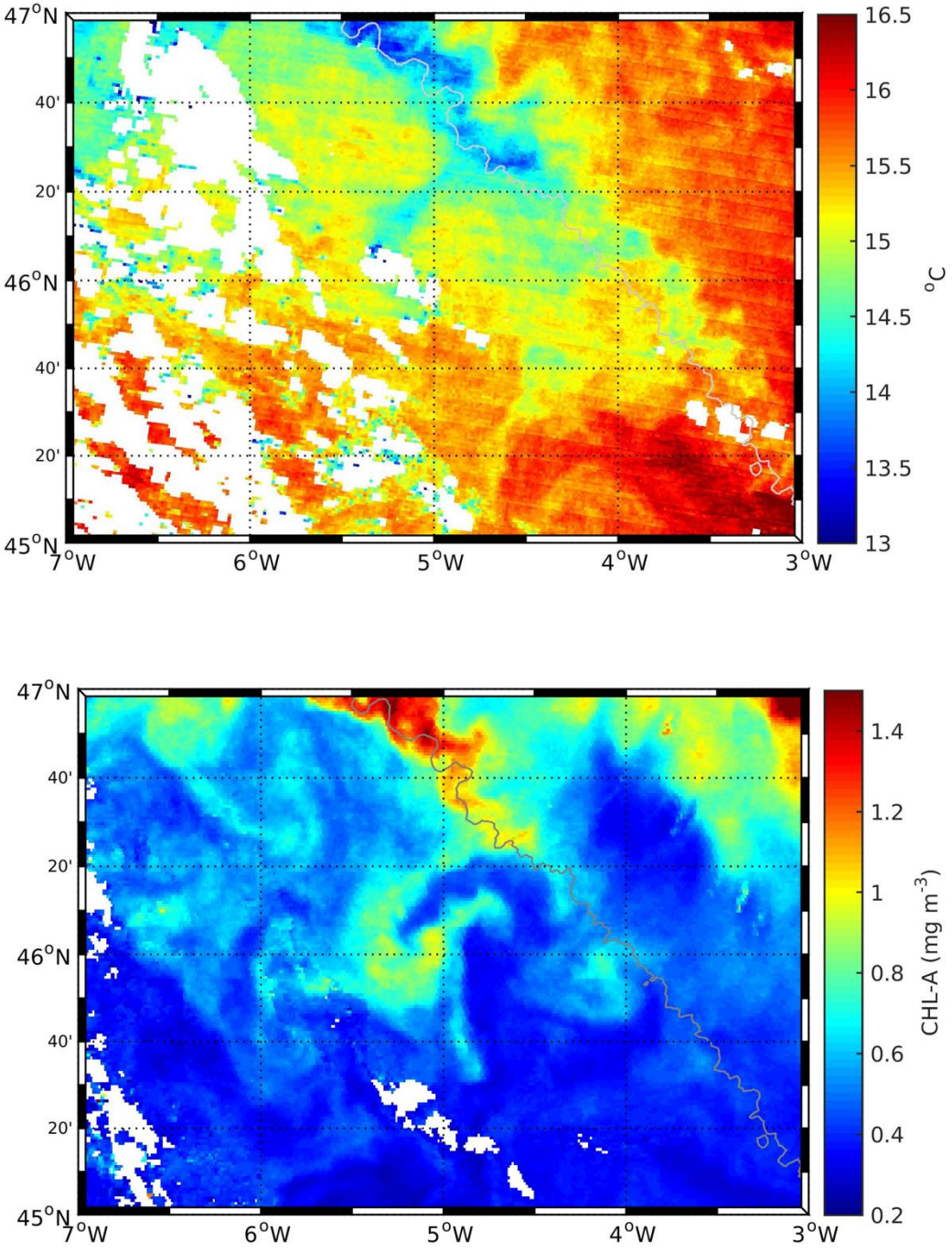

491

492 Figure 11. Remotely sensed sea-surface temperature (top) and chlorophyll-*a* concentrations

493 (bottom) on 20 May 2008.

494

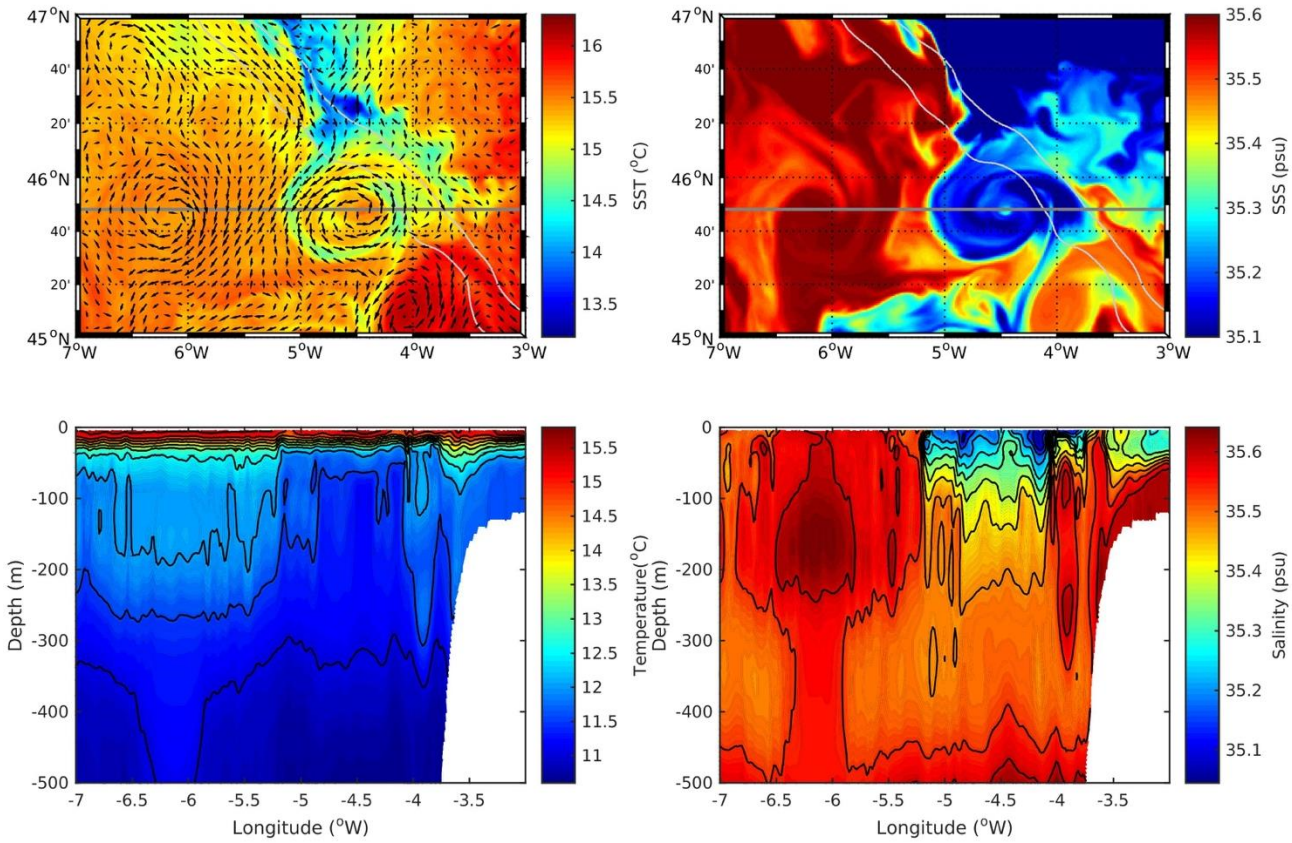

Figure 12. Simulated fields on 26 May 2008. Surface velocity field superimposed on sea surface temperature (top left), sea surface salinity (top right). Gray line in the top panel represents the 45.8°N transect. The vertical temperature transect (bottom left) and the vertical salinity transect (bottom right) along 45.8°N.

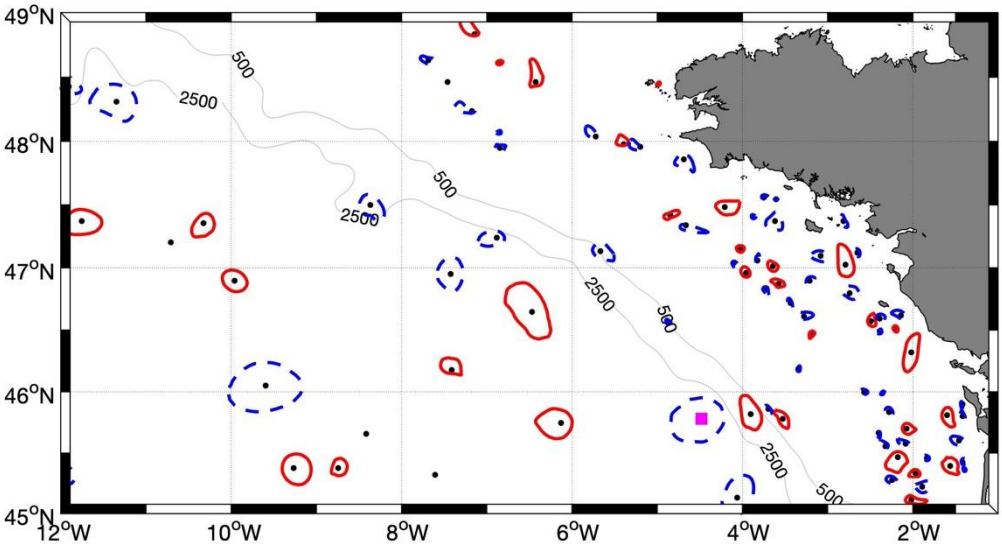

Figure 13. Eddy distribution on 26 May 2008. Anticyclonic eddies are denoted by red circles and cyclonic eddies by blue dashed circles. Black dots are the eddy centers. The center of the cyclonic eddy detailed in the text is indicated with a filled magenta square.

3.4 Contribution of wind forcing to cross-shelf exchanges

Wind-induced transport is another important mechanism to consider for cross-shelf exchanges. In this section, we investigate potential impacts of wind on cross-shelf exchanges.

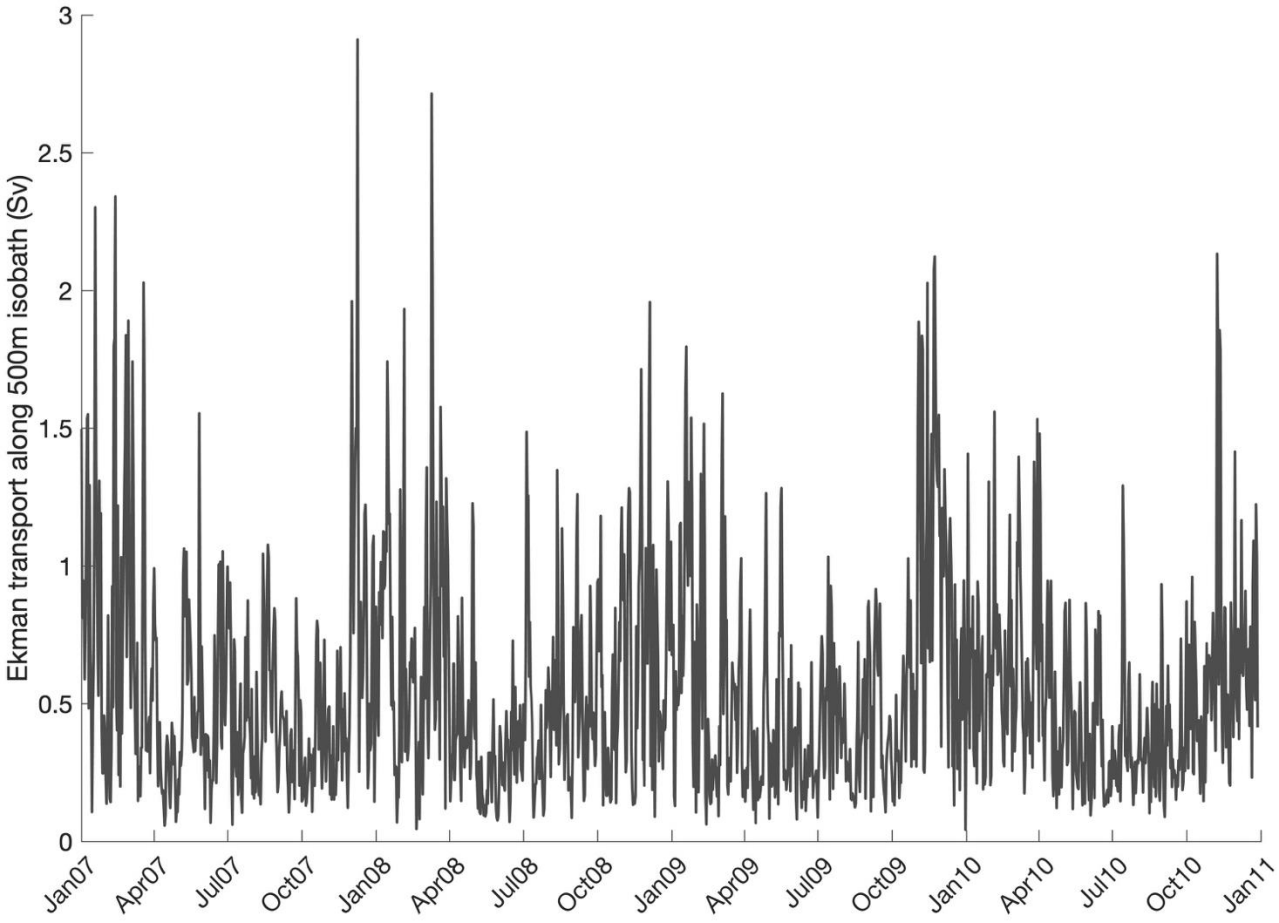

509

510 Figure 14. Ekman transport (Sv) along the 500 m isobath for 2007-2010.

511

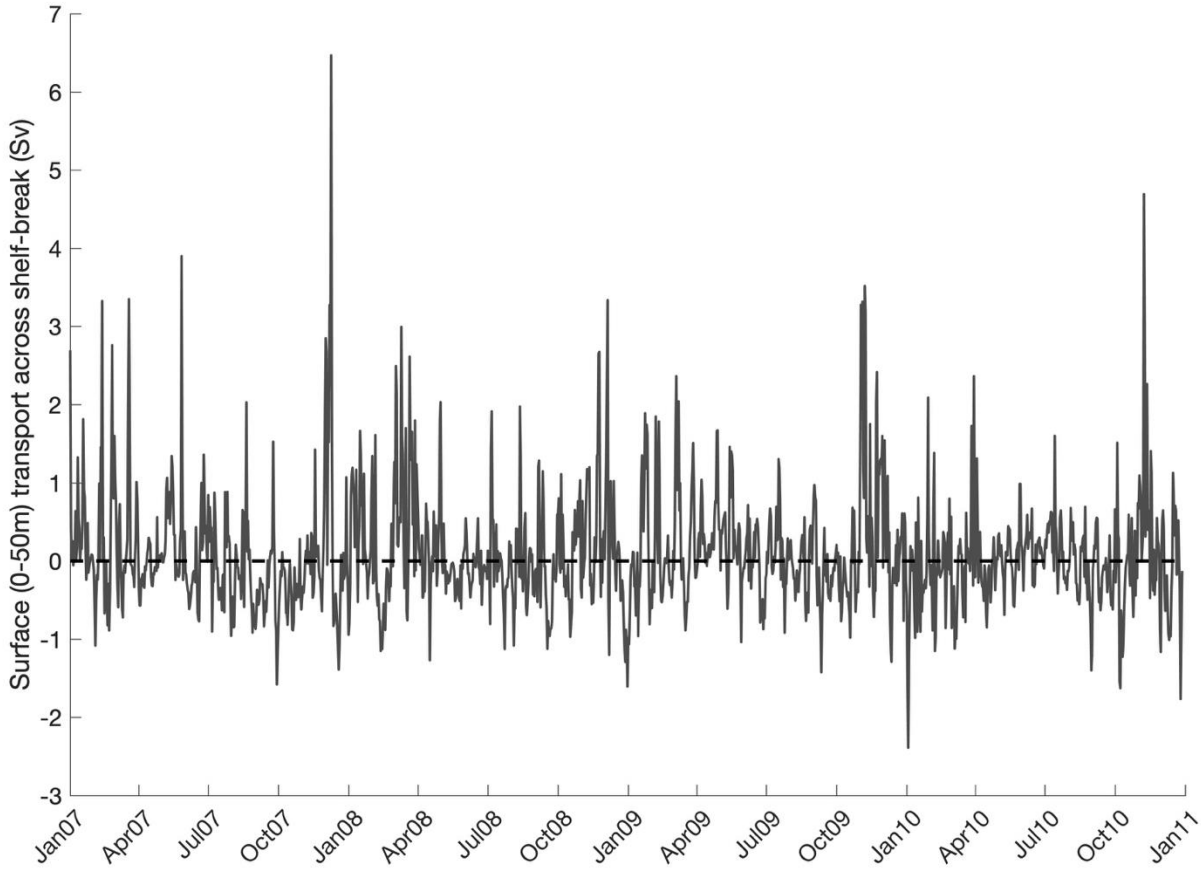

Figure 15. 0-50 m net transport (Sv) integrated over the 500 m isobath (red line in Figure 1). Positive values denote downslope transport and negative values represent upslope transport.

The daily evolution of the Ekman transport averaged over 500 m isobath is given in Figure 14. Depending on the wind speed, Ekman transport values can exceed 2.5 Sv. Similarly, Ekman depth ranged from 20 m (in summer) to up to ~100 m in winter. Annual mean Ekman depth ranged from 40 to 46m, with a 2007-2010 average of 44 m depth.

Eddies are ubiquitous features of the circulation. Thus, it is not straightforward to show wind-induced (Ekman) transport only in the presence of eddies based on realistic numerical simulations. Taking into account the high variability of the Ekman depth, we present the total shelf-break transport at 0-50 m (Figure 15), as well as the Ekman transport (Figure 14). Mean net Ekman transport (Figure 14) and 0-50 m transport (Figure 15) were correlated (0.57), suggesting that the surface (0-50 m) transport is partially explained by wind-induced transport.

526 The 0-50 m volume transport across the shelf break displayed oscillations both upslope and
527 downslope, with larger magnitudes (positive values) in downslope transport.
528
529 Figure 13 shows that the strongest upslope transport event took place on 3 January 2010. This
530 day had the strongest winds of a period with northwestward winds (Figure 16), which resulted
531 in strong upslope transport. Observed extreme values (both upslope and downslope) with the
532 strongest wind magnitudes generally led to downslope transports.
533
534 Based on available satellite data, we present an example of a downslope transport case that
535 occurred as a result of both Ekman transport and eddy-induced transport. On 18 July 2010,
536 eastward wind generated surface Ekman transport towards the south (Figure 17). Although
537 limited in space and time, satellite sea-surface temperatures (Figure 18) suggest a spreading of
538 colder waters towards south. During the months when the seasonal stratification develops, most
539 satellite sea-surface temperature maps show a cold water band at the shelf break resulting from
540 mixing via internal tides (e.g. Pingree et al., 1986; New, 1988).
541 However, during this event (Figure 18), cold waters extended downslope. Presence of an eddy
542 (centered at 46^{o}N, 5.5^{o}W) also enhanced this cross-shelf export. This event was successfully
543 simulated in the model, representing the spreading of the cold water band downslope.
544 Simulations also corroborated satellite data by showing that this spread of cold waters was not
545 just due to wind, but also to eddies generated along the shelf-break. On the other hand, in the
546 model, eddies were generated at different locations. Starting from 15 July 2010, a cyclonic
547 shelf-break eddy was simulated (at 47.5°N-7.5°W) and it progressed southeastward along the
548 shelf break, contributing to the downslope transport (Figure 19 and Figure 20). Another
549 cyclonic eddy and associated filament (~47°N-5.5°W) contributed to the downslope transport.
550 Transport of fresher waters via the eddy was clearly observed on the surface salinity map

(Figure 20), as well as the spreading of colder waters downslope in the sea-surface temperature distribution.

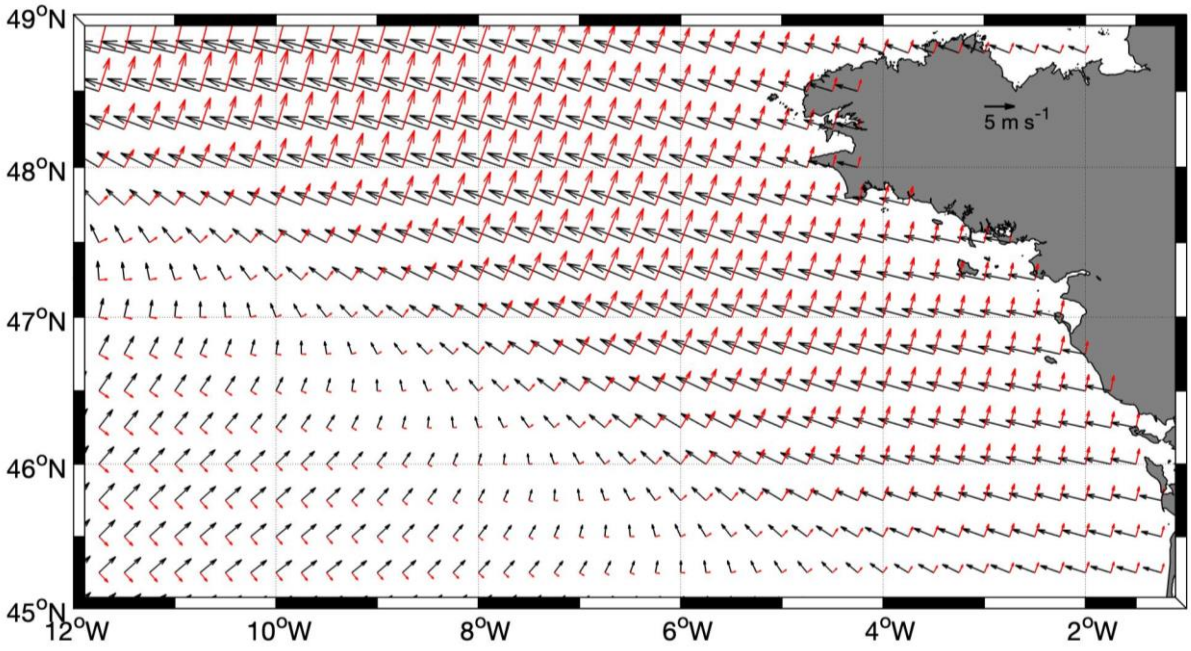

Figure 16. Wind direction (black arrows) and Ekman transport direction (red arrows) on 3 January 2010.

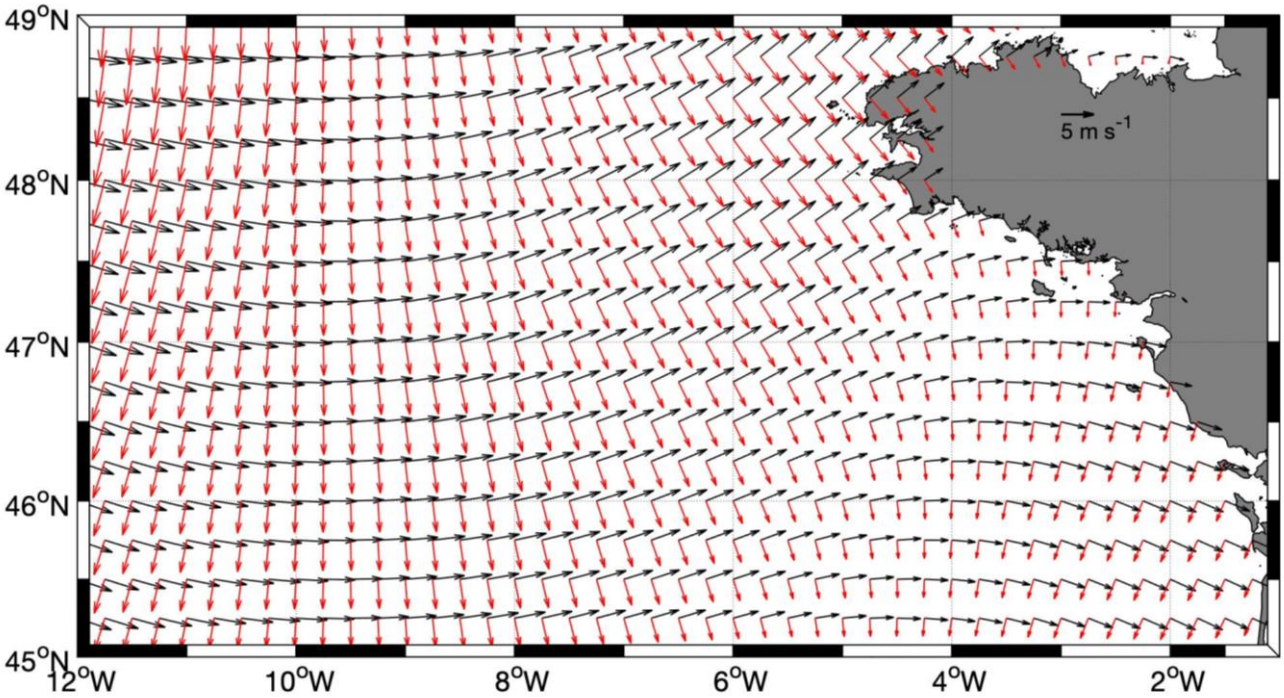

559

560 Figure 17. Wind direction (black arrows) and Ekman transport direction (red arrows) on 18 July

561 2010.

562

563

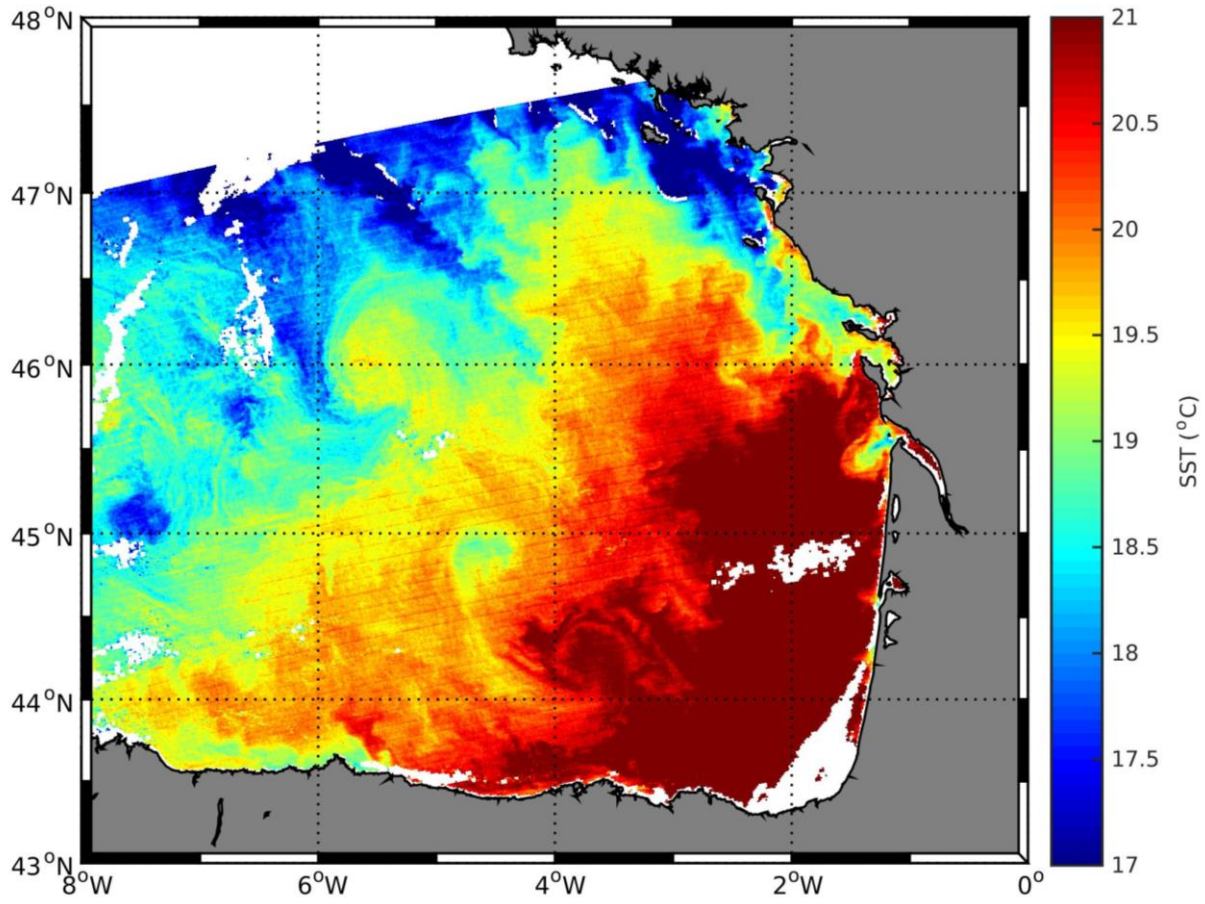

564

565 Figure 18. MODIS remotely sensed sea surface temperature on 18 July 2010.

566

567

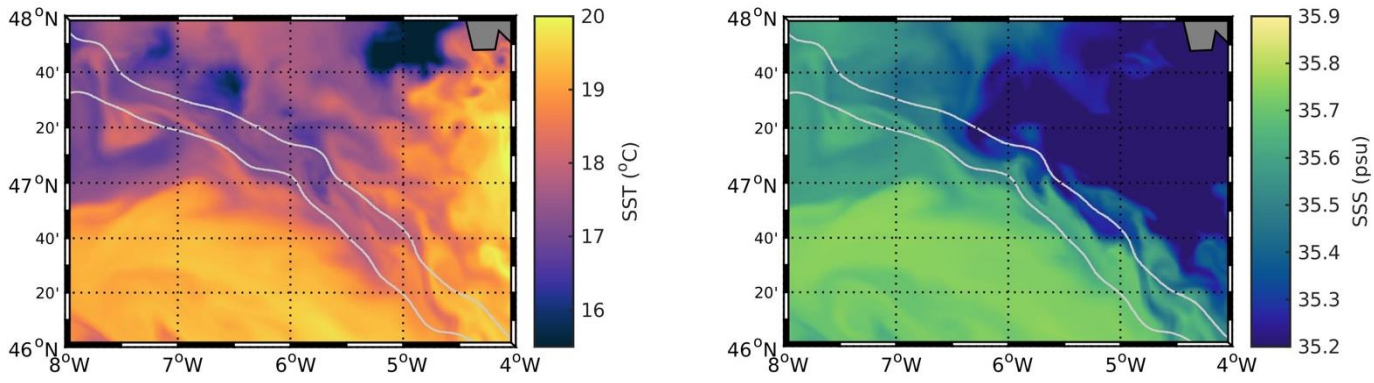

568

569 Figure 19. Simulated sea-surface temperature (left) and sea surface salinity (right) on 20 July

570 2010.

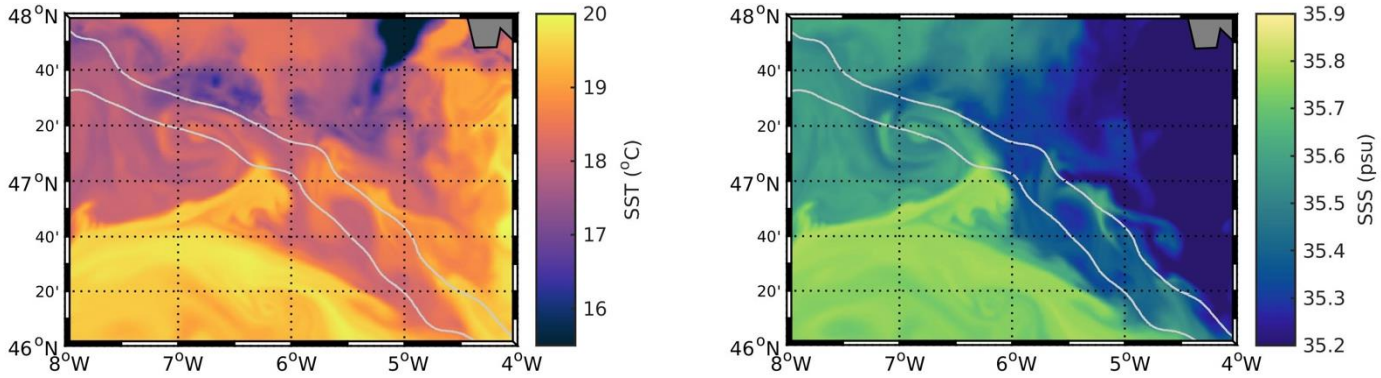

Figure 20. Simulated sea surface temperature (left) and sea surface salinity (right) on 31 July 2010.

4. Discussion

Shelf-break circulation

Here, we compared along-shelf and cross-shelf flows to demonstrate the accuracy of our simulations and to emphasize that the major along-slope transport is well-reproduced in high resolution (1 km resolution) simulations. Modelled along-shelf velocity was between 0.1 and 0.25 m s^{-1}, which is consistent with previous observations of the slope current around 0.1-0.3 m s^{-1} (Huthnance et al., 1999; Pingree et al., 1999; Le Boyer et al., 2013) and simulations of similar resolution (Graham et al., 2018). In terms of slope current direction, simulations corroborated previous observations of seasonal reversal of the main current direction (Charria et al., 2013; Porter et al., 2016), flowing poleward in winter and equatorward in summer, as circulation resulting from the SOMA (September/October-March/April) effect (Pingree et al., 1999).

Due to the dominant slope current dynamics, cross-shelf currents (ranging between 3 cm s^{-1} and 10 cm s^{-1}) are less intense than along-shore. However, cross-shelf currents can occasionally

become dominant. These local intensifications can be explained by the presence of eddies and local eddy interactions generating filaments.

Overall cross-shelf transports

Based on these simulated currents, the cross-shelf transports can be quantified and compared with previous estimations based on coarser resolution models. Huthnance et al. (2009) simulated an average transport (at 48^{o}N) of 0.2 Sv (upslope) above 150 m depth and 0.01 Sv (downslope) below 150 m. Based on our analysis, we extend this estimation further south in the Bay of Biscay with a more detailed view on cross-shelf transports. Cross-shelf transport estimates were recently detailed for an adjacent, partially overlapping region (Graham et al., 2018).

For surface transports (0-20 m), two models with different resolution (1.5 km and 7 km) gave estimates of 0.52 Sv and 0.54 Sv net upslope transport, respectively, similar to our estimation of 0.5 Sv over the shelf break. Importantly, the region of interest partially coincides, where the southern boundary of their region (Graham et al., 2018) corresponds to the northern boundary of ours. Therefore, direct comparison of transport estimates is not possible. However, transport estimates are of the same order of magnitude, and have similar directions, corroborating our estimations. Additionally, the largest volume transports were observed (red line, Figure 3) in winter and the lowest transports in summer, matching the Graham et al. (2018) comparisons for January and July. Such upslope surface transports have also been simulated by Holt et al. (2009) in the Celtic Sea region with values of 0.26 Sv in the upper 180 m depth combined with downslope surface transports (0.14 Sv) in the Biscay region. Our higher resolution simulation confirms downslope surface transport (about 0.6 Sv) in the Bay of Biscay.

615

616 **Temporal evolution of cross-shelf transports**

617 The temporal evolution of vertically integrated cross-shelf exchange along the 500 m isobath
618 is shown in Figure 3. Spectral analysis of the oscillating signal highlights 14-day and 28-day
619 frequencies. These are clearly the imprints of the lunar fortnightly and lunar monthly tidal
620 components. This is an expected result, because we conducted our analysis on daily-averaged
621 data, which filters out short-term tidal components (e.g. M2, S2, K1, O1). To show the longer-
622 term signal, we filtered the time-series with a moving average (31-day moving window).
623 On these filtered time-series, larger negative velocities were simulated in winter 2010. This
624 specific year was associated with a cold winter and deep winter mixed layers (Hartman et al.,
625 2014; Charria et al., 2017). During winter 2010, the overall dynamics (e.g. vertical velocities,
626 relative vorticity) were more active (Charria et al., 2017), inducing an amplification of upslope
627 slope circulation. In contrast, winter 2008 was a mild winter (Hartman et al., 2014) and appears
628 as the winter with the least intense upslope fluxes of the study period.
629 To evaluate long-term evolution, an extended simulation should be used and analyzed in detail,
630 exploring impacts of other possible large-scale factors (e.g. stability of the slope current,
631 atmospheric regimes such as the North Atlantic Oscillation).
632

633 **The vertical structure of cross-shelf transports**

634 The vertical structure of the cross-shelf transports can be divided into three vertical layers.
635 These three layers appeared clearly in our simulations. They represent an imprint of mesoscale
636 eddies and wind-induced Ekman transport for the upper layer, mesoscale eddies for the mid-
637 layer and an “Ekman drain” (Simpson and McCandliss, 2013) for the bottom boundary layer.
638

639

640 The bottom boundary layer

641 An important process demonstrated in previous studies (Maas and Zimmermann 1989; Lam et
642 al., 2004) is the subsurface intensification of the mean along-shelf flow, which was associated
643 with frictional modification of tidally rectified flow (Lam et al., 2004). In our simulations,
644 subsurface intensification of along-slope flow was observed over the shelf-break, but generally
645 at shallower depths (less than 200-300 m), corroborating earlier results (Pingree and Le Cann
646 1989; Lam et al., 2004). Deeper in the water column, a persistent downslope cross-shelf flow
647 was observed. This downslope flow, also named the Ekman drain, has been observed and
648 simulated in various past studies (Pingree and Le Cann, 1989; Butman, 1988; Souza et al., 2001;
649 Holt et al., 2009; Simpson and McCandliss, 2013). In our simulation, the time-series of this
650 flow showed oscillation with frequencies of tidal constituents. As suggested by Butman (1988),
651 this bottom flux, related with frictional effects, can be sustained by tidal oscillations.

652 This cross-shelf flow at the bottom boundary was found to reach its maximum at the 500 m
653 contour, with typical values of 0.1 m s^{-1} downslope, occasionally reaching 0.2 m s^{-1}. This flow
654 accounts for about 10% of the total cross-shelf transport. These simulations are coherent with
655 previous field measurements of bottom currents, with reports of residual currents increasing to
656 0.1 m s^{-1} near the shelf break and maximal bottom currents near the 500 m contour with an
657 average of 0.14 m s^{-1} (Pingree and Le Cann, 1989).

658 A clear feature observed in our simulations is the enhancement of the bottom boundary cross-
659 shelf flow near Chapel Bank (Figure 4 and Figure 5).). In this region, the slope current is
660 stronger (Pingree and Le Cann, 1989), enhancing the intensity of bottom boundary flow related
661 with the “Ekman drain” . We initially chose the 500 m isobath because it represents the core
662 of the slope current (Xu et al.,2015).

663 To infer the variability of cross-shelf flow along the shelf break (downslope direction), we also
664 investigated the bottom flow at 1000 m. The bottom boundary did not persist at 1000 m. Thus,

665 it was not directly comparable to the bottom boundary flow at 500 m. However, one similarity
666 with the 500 m isobath is the localized intense bottom boundary flow observed between 47^{o}N
667 and 48^{o}N. This feature can be linked to the topographic features (i.e. canyons) in the region, as
668 previously speculated by others (Codiga et al., 1999; Lam et al., 2004). We found a gradual
669 decline in the bottom boundary flow downslope (towards 1000 m).
670 Recently, Graham et al. (2018) suggested slope current seasonality and bathymetry as possible
671 factors contributing to the strength and variability of bottom fluxes. Similar to our findings,
672 they reported spatial variability in the bottom fluxes (i.e. intensity and thickness of the bottom
673 boundary) related to the above along-shelf slope current. Idealized experiments are needed to
674 understand the relative contribution of the various terms (e.g. stratification, topography, bottom
675 friction, internal tides) on the bottom boundary cross-shelf flow.
676 Although bottom boundary cross-shelf exchanges represent smaller magnitudes than the
677 surface cross-shelf exchanges, especially in the presence of eddy-driven exchanges and/or
678 wind-driven exchanges, it is still an important part of cross-shelf exchanges because it is
679 permanent. Thus, it becomes a major component of cross-shelf exchanges in the absence (or
680 weak states) of eddy-driven and/or wind-driven cross-shelf exchanges.
681
682 <u>The contribution of mesoscale dynamics to cross-shelf exchanges</u>
683 Eddy-driven cross-shelf transport has been suggested to be a key mechanism for cross-shelf
684 exchanges in the southern (Reverdin et al., 2013; Rubio et al., 2018) and northern part of the
685 Bay of Biscay (Porter et al., 2016). Small anticyclonic eddies arising from slope topography
686 has been shown to be a mechanism for on-shelf transport (Porter et al., 2016). Following a
687 similar approach to these studies, investigating satellite sea-surface temperature and
688 chlorophyll-*a* maps, we identified various cross-shelf exchange events. Interestingly, we
689 identified not only anticyclonic eddies, but also cyclonic eddies (60% of total eddies), as well

as eddy dipoles in some cases, contributing to cross-shelf exchanges. To further investigate these events, we explored simulations with 2.5 km and 1 km resolutions. Although successful for large-scale eddies (>10-15 km), the 2.5 km resolution simulations were not able to reproduce small-scale shelf-break eddies (<10 km). Thus only the 1 km simulations were used to investigate cross-shelf exchange events. With a similar approach, a recent study (Graham et al., 2018) compared 1.5 km and 7 km resolution simulations, concluding on the necessity for higher resolution to resolve cross-shelf exchanges, which can only be resolved starting from the O(1 km). From this perspective, our results emphasize the need for higher resolution models to resolve cross-shelf exchanges.

One concern regarding high-resolution models is the successful reproduction of submesoscale features. It is possible to under- (or over-)estimate these small-scale features. The model used in this study had been validated previously (Charria et al.,2017), showing that the model can successfully reproduce field measurements of along-shelf and cross-shelf velocities. Also, the model successfully reproduced most of the features observed in satellite maps. An example is clearly seen in Figure 11, where there is a secondary eddy located at 46^{o}N, 4.5^{o}W, which was also successfully simulated as shown in Figure 12. Based on these examples, we confirm that the model can reproduce eddy activity in this dynamically complex slope region. However, the validation of mesoscale and submesoscale processes remains a challenging issue in regions such as the Bay of Biscay, where remotely sensed observations are sparse due to cloud contamination and close shelf regions (limitation for altimetry). Another important factor for characterizing the eddy field is the eddy-tracking algorithm applied on the simulated velocity field. Although there are numerous eddy-detection and -tracking algorithms available, we demonstrated that AMEDA (Le Vu et al.,2018) is suitable for the purpose of this study. Another important advantage of this algorithm is that it requires a limited number of tunable parameters.

715 The initial parameter (see grid parameter in Le Vu et al.,2018) to detect the eddies depends on
716 the Rossby radius of deformation (Rd). This radius is important to precisely detect shelf-break
717 eddies, considering the rapid changes of Rd over the shelf break. Eddy tracking was used to
718 obtain the general characteristics of eddies (number, size, tracks etc.) to investigate their impact
719 on the cross-shelf fluxes.
720 The eddy presence map (Figure 7) shows that eddy presence south of 47.5°N was concentrated
721 along the 500 m contour, whereas eddy presence north of 47.5°N was concentrated near the
722 2500 m contour. This can be linked to the complex bathymetry (canyons) south of 47.5°N, as
723 well as to smaller Rd values, leading to the generation and propagation of smaller eddies in this
724 region. Minimum eddy frequency along the shelf break was observed between the 2500 m and
725 4000 m contours (between 5°W-7°W and 46°N-46.5°N) with almost no eddy presence (less than
726 5%). This can be explained by the propagation of smaller eddies along the (southern or
727 northern) slope . Thus, although there are some eddies in this region, their presence over time
728 is minimal.
729
730 The number of eddies peaked in July-October and dipped in December-April, meaning the
731 number of eddies was maximal during the stratified period. In 2008, there were 475 eddies in
732 the study domain (magenta box in Figure 1), of which 282 were cyclonic and 193 were
733 anticyclonic. Although the number of cyclonic eddies was generally higher (60% of total
734 number of eddies) than the number of anticyclonic eddies in the study period, there was no
735 significant correlation between shelf-break cyclonic/anticyclonic eddies and the magnitude or
736 direction of the cross-shelf fluxes. Cross-shelf fluxes reached their maximum positive values
737 (downslope) when the number of shelf-break eddies were at their lowest and their lowest
738 negative values (upslope) when the number of shelf-break eddies reached their maximum.
739 There was no significant correlation between the number of shelf-break eddies and the cross-

shelf transport below the surface (50-350 m). This lack of association at the subsurface partly arises from the fact that the eddy-tracking algorithm was applied on the surface velocity field and does not consider subsurface circulation. Also, subsurface cross-shelf fluxes are influenced by other factors (such as internal tides), which may have a larger impact.

Eddy activity was associated with eddy-induced transport (comparison between mesoscale filtered simulation and initial simulation) contributing to about 30% of the total cross-shelf transport. The eddy contribution to cross-shelf exchanges tends to limit the export of shelf water with a stronger impact on upslope transport (eddy-induced circulation contributes to 40% of the upslope transport and 27% of the downslope transport). This overall quantification of the impact of mesoscale circulation on cross-shelf transport shows the importance of eddies in this intermediate shelf-break region on the export of shelf water masses.

Wind forcing: the surface controller of cross-shelf exchanges

In the Bay of Biscay, the general wind patterns were shown to be southeastward in summer and northeastward in winter with two transition periods in September/October and March/April (Le Boyer et al., 2013). As confirmed in Le Boyer et al. (2013), we observed strong northward winds in 2010, which resulted in enhanced cross-shelf transport at the surface layer (Figure 16 and Figure 17). A case from winter 2010 was illustrated (Figure 16), as well as a case observed in summer 2010 (Figure 17). Both cases show situations of strong winds with opposite effects. In the case of July 2010 (Figure 17), cold waters were transported downslope to the south, and an eddy contributing to this transport was also present.

It is not straightforward to distinguish between wind-induced and eddy-induced cross-shelf transport at the surface, because eddies are ubiquitous features of the circulation. For this case (Figure 18), the eddy was reproduced with a lag in the model. A specific study is required to determine eddy generation over the shelf break, as well as the response to the wind field.

765 With Ekman transport reaching 2.5 Sv at the surface, wind accounts for 60% of cross-shelf
766 transport in the 0-50 m surface layer.
767
768
769 **5. Conclusions**
770 In the Bay of Biscay, along the 500 m isobath, average (2007-2010) downslope transport was
771 1.17 Sv and upslope flux was -1.74 Sv. To differentiate contributions from different processes
772 (e.g. eddies, wind, bottom Ekman drain), we investigated three layers of the water column
773 separately. For the surface layer (0-50 m), the average downslope flux was 0.6 Sv and upslope
774 flux was -0.38 Sv. Wind and eddies are the two main factors affecting the surface layer. In this
775 surface layer, wind forcing accounts for 60% of the cross-shelf transport and eddy activity
776 accounts for 30%.
777 Below the surface layer, a uniform layer (no sign changes) extends down to the bottom layer.
778 For this layer (50 m-400 m), the average downslope flux was 0.5 Sv and upslope flux was -1.84
779 Sv. We identified eddies to be the main factor affecting these fluxes.
780 Finally, the bottom-boundary layer (400 m-500 m) displays an average downslope flux of 1 Sv
781 and upslope flux of -0.1 Sv. This “Ekman drain” related to slope current dynamics contributes
782 to 10% of the total cross-shelf transport.
783 Average values, as well as the time-series, suggest that the downslope transport prevails at the
784 surface and near-bottom layers in the region, whereas at mid-depths, the transport is upslope.
785 Considering that depths between 50 m-400 m represent 70% of the total water column, this
786 layer accounts for the overall upslope cross-shelf transport (red line in Figure 1, Table 1).
787
788 Cross-shelf exchanges were quantified and detailed according to different drivers (eddies,
789 frictional effects due to wind and slope current/bathymetry interaction). Other mechanisms can

contribute to cross-shelf exchanges, such as internal waves (Hopkins et al., 2012), but they affect cross-shelf transport on shorter time scales. Exploring the contribution of these short-term processes will need dedicated experiments with higher resolution to improve the modelling of internal tides.

This study demonstrates the need for high-resolution simulations for investigating shelf-break eddies and ocean-shelf exchanges. Additionally, our model and eddy-tracking algorithm emphasize the importance of shelf-break resolution. We were able to resolve many different dynamics with a 1 km resolution. However, higher resolution models (higher resolution at the shelf break), can be employed in particular to resolve submesoscale eddies, internal tide dynamics and to understand the impact of the complex bathymetry (canyons) in this region. Our results suggest that shelf-break eddies are formed near canyons. Ideally, idealized simulations should be used to test different forcings. These simulations are necessary to understand eddy formation, propagation and interactions with complex bathymetry, as well as to better understand cross-shelf dynamics in this region.

Acknowledgements

This study received funding from the European Union's Horizon 2020 AtlantOS Project and IFREMER. This study is part of the COCTO project (SWOT Science Team Program) funded by the CNES. Model simulations were carried out with GENCI (French National High-Performance Computing Organization) computational resources administered at the CINES (National Computing Center for Higher Education). We thank Bernard Le Cann for his constructive comments and fruitful discussions, which greatly improved this study. We also thank the anonymous referees for their insightful and thoughtful comments.

References

Badin, G., Williams, R. G., Holt, J. T., Fernand, L. J., (2009). Are mesoscale eddies in shelf seas formed by baroclinic instability of tidal fronts ? Journal of Geophysical Research-Oceans, 114(October), 1–18. http://doi.org/10.1029/2009JC005340

Brink, K. H. (2016). Cross-shelf exchange. *Annual Review of Marine Science* 8, 59–78. doi: 10.1146/annurev-marine-010814-015717

Butman, B., 1988: Downslope Eulerian mean flow associated with high-frequency current fluctuations observed on the outer continental shelf and upper slope along the northeastern United States continental margin: Implications for sediment transport. *Cont. Shelf Res.*, **8**, 811–840, doi:https://doi.org/10.1016/0278-4343(88)90078-7.

Caballero, A., Ferrer, L., Rubio, A., Charria, G., Taylor, B. H., Grima, N., (2014). Monitoring of a quasi-stationary eddy in the Bay of Biscay by means of satellite , in situ and model results. Deep-Sea Research Part II, 106, 23–37. http://doi.org/10.1016/j.dsr2.2013.09.029

Chaigneau, A., A. Gizolme, Grados C., (2008). Mesoscale eddies off Peru in altimeter records: Identification algorithms and eddy spatio-temporal patterns. Progress in Oceanography., 79 (2–4), 106–119. http://doi.org/10.1016/j.pocean.2008.10.013

Charria G., Lazure P., Le Cann B., Serpette A., Reverdin G., Louazel S., Batifoulier F., Dumas F., Pichon A., Morel,Y., (2013). Surface layer circulation derived from Lagrangian drifters in the Bay of Biscay. Journal of Marine Systems, 109-110, S60–S76.

http://doi.org/10.1016/j.jmarsys.2011.09.015

Charria, G., Theetten, S., Vandermeirsch, F., Yelekçi, Ö., Audiffren, N., (2017). Interannual evolution of (sub) mesoscale dynamics in the Bay of Biscay, Ocean Science, 13(5), 777-797. https://doi.org/10.5194/os-13-777-2017

Cherian, D. A. and Brink, K. H., (2016). Offshore Transport of Shelf Water by Deep-Ocean Eddies, Journal of Physical Oceanography., 46, 3599–3621, https://doi.org/10.1175/JPO-D-16-0085.1

Codiga, D.L., Renouard, D.P., Fincham, A.M., (1999). Experi- ments on waves trapped over the continental slope and shelf in a continuously stratified rotating ocean, and their incidence on a canyon. Journal of Marine Research 57 (4), 585–612. https://doi.org/10.1357/002224099321549602

Combes, V., Chenillat, F., Lorenzo, E. Di, Rivière, P., Ohman, M. D., Bograd, S. J., (2013). Cross-shore transport variability in the California Current : Ekman upwelling vs . eddy dynamics. Progress in Oceanography, 109, 78–89. http://doi.org/10.1016/j.pocean.2012.10.001

Dumas, F., Pineau-Guillou, L., Lecornu, F., Le Roux, J.-F., Le Squere, B., 2014. General Introduction: PREVIMER, a French pre-operational coastal ocean forecasting capability. Mercato. Ocean-Q. Newsl., 3–8.

Frankignoulle, M., Borges, A. V., (2001). European continental shelf as a significant sink for

865 atmospheric carbon dioxide. Global Biogeochemical Cycles,15, 569–576.
866 https://doi.org/10.1029/2000GB001307
867
868 Garcia-soto, C., Pingree, R.D., Valdes,L., (2002). Navidad development in the southern Bay of
869 Biscay : Climate change and swoddy structure from remote sensing and in situ
870 measurements. Journal of Geophysical Research-Oceans ,107, 1–29.
871 https://doi.org/10.1029/2001JC001012.
872
873 Gohin, F., Saulquin, B., Oger-Jeanneret, H., Lozac'h, L., Lampert, L., Lefebvre, A., Riou, P.,
874 and Bruchon, F., (2008). Towards a better assessment of the ecological status of coastal waters
875 using satellite-derived chlorophyll-a concentrations, Remote Sensing of Environment, 112,
876 3329-3340, https://doi.org/10.1016/j.rse.2008.02.014
877
878 Graham, J. A., Rosser, J.,P., O'Dea, E., Hewitt, H. T., (2018). Resolving shelf-break exchange
879 around the European north-west shelf. Geophysical Research Letters, 45(22),12386-
880 12395, http://doi.org/10.1029/2018GL079399.
881
882 Gruber, N. (2014). Ocean biogeochemistry: Carbon at the coastal interface, Nature, 517, 148–
883 149. http://doi.org/10.1038/nature14082
884
885 Hartman, S. E., g, M. C., Hydes, D. J., Jiang, Z.-P., Smythe-Wright, D., and González-Pola, C.
886 (2014). Seasonal and inter- annual variability in nutrient supply in relation to mixing in the Bay
887 of Biscay, Deep-Sea Res. Pt. II, 106, 68–75, https://doi.org/10.1016/j.dsr2.2013.09.032
888
889 Holt, J.T., Wakelin S.L., Huthnance, J.M. (2009). The downwelling circulation of the northwest

890 European continental shelf: a driving mechanism for the continental shelf carbon pump.
891 Geophys Res Lett 36, L14602. doi:10.1029/2009GL038997
892
893 Hopkins, J., Sharples, J., Huthnance, J. M., (2012). On-shelf transport of slope water lenses
894 within the seasonal pycnocline, Geophysical Research Letters,39(8), L08604,
895 http://doi.org/10.1029/2012GL051388
896
897 Hu, C., Z. Lee, and B.A. Franz, (2012). Chlorophyll-a algorithms for oligotrophic oceans: A
898 novel approach based on three-band reflectance difference, J. Geophys. Res., 117, C01011,
899 doi:10.1029/2011JC007395.
900
901 Huthnance, J. M., (1995). Circulation, exchange and water masses at the ocean margin: the role
902 of physical processes at the shelf edge, Progress in Oceanography, 35, 353–431,
903 doi:10.1016/0079-6611(95)80003-C.
904
905 Huthnance, J. M., H. M. Van Aken, M. White, E. D. Barton, B. Le Cann, E. F. Coelho, E. A.
906 Fanjul, P. Miller, and J. Vitorino, (2002). Ocean margin exchange-water flux estimates, Journal
907 of Marine Systems, 32, 107–137, https://doi.org/10.1016/S0924-7963(02)00034-9
908
909 Huthnance, J. M., Holt, J. T., Wakelin, S. L., (2009). Deep ocean exchange with west-European
910 shelf seas.Ocean Science, 5: 621–634. https://doi.org/10.5194/os-5-621-2009
911
912 Kersalé, M., Marié, L., Le Cann, B. , Serpette, A. , Lathuilière, C., Le Boyer, A., Rubio, A.
913 and Lazure, P. (2016). “Poleward along-shore current pulses on the inner shelf of the Bay
914 of Biscay”, *Estuarine, Coastal and Shelf Science*, 176, pages 155–171.

https://doi.org/10.1016/j.ecss.2015.11.018

Lam, F. P. A., Maas, L. R. M., and Gerkema, T., (2004). Spatial structure of tidal and residual currents as observed over the shelf break in the Bay of Biscay, Deep-Sea Res., Part I, 51, 1075–1096, https://doi.org/10.1016/j.dsr.2004.03.008

Lazure, P., Dumas, F. (2008). An external–internal mode coupling for a 3D hydrodynamical model for applications at regional scale (MARS). Adv. Water Resour., 31, 233–250, https://doi.org/10.1016/j.advwatres.2007.06.010.

Le Boyer, A., Charria, G., Le Cann, B., Lazure, P., and Marié, L. (2013). Circulation on the shelf and the upper slope of the Bay of Biscay, Cont. Shelf Res., 55, 97–107, https://doi.org/10.1016/j.csr.2013.01.006

Leblond E., Lazure P., Laurans M., Rioual C., Woerther P., Quemener L., Berthou P. (2010). The RECOPESCA project: A new example of participative approach to collect fisheries and in situ environmental data. CORIOLIS Quarterly Newsletter (Mercator Ocean), 2010-04 , N. 37 , P. 40-48. 37.

Le Vu, B., Stegner, A., and Arsouze, T.(2018). Angular Momentum Eddy Detection and tracking Algorithm (AMEDA) and its application to coastal eddy formation, Journal of Atmospheric and Oceanic Technology, 35(4), 739-762, https://doi.org/10.1175/JTECH-D-17-0010.1

939 Maas, L.R.M., Zimmerman, J.T.F., (1989). Tide-topography interactions in a stratified shelf
940 sea II. Bottom trapped internal tides and baroclinic residual currents. Geophysical and
941 Astrophysical Fluid Dynamics 45, 37–69. https://doi.org/10.1080/03091928908208892
942
943 Manso-Narvarte, I.; Caballero, A.; Rubio, A.; Dufau, C.; Birol, F (2018). Joint analysis of
944 coastal altimetry and high-frequency (HF) radar data: Observability of seasonal and mesoscale
945 ocean dynamics in the Bay of Biscay. *Ocean Science*, *14*, 1265–
946 1281. https://doi.org/10.5194/os-14-1265-2018
947
948 Marchesiello, P., Debreu, L., and Couvelard, X. (2009). Spurious diapycnal mixing in terrain-
949 following coordinate models: The problem and a solution. Ocean Modelling, 26(3-4), 156-169.
950 https://doi.org/10.1016/j.ocemod.2008.09.004
951
952 Mkhinini, N., A. L. S. Coimbra, A. Stegner, T. Arsouze, I. Taupier-Letage,
953 and K. Béranger, (2014). Long-lived mesoscale eddies in the eastern Mediterranean Sea:
954 Analysis of 20 years of AVISO geostrophic velocities. *J. Geophys. Res. Oceans*, 119, 8603–
955 8626, https://doi.org/10.1002/2014JC010176.
956
957 Nencioli, F., Dong, C., Dickey, T., Washburn, L., and McWilliams, J. C. (2010). A Vector
958 Geometry-Based Eddy Detection Algorithm and Its Application to a High-Resolution
959 Numerical Model Product and High-Frequency Radar Surface Velocities in the Southern
960 California Bight, J. Atmos. Ocean. Tech., 27, 564–579, doi:10.1175/2009JTECHO725.1
961

962 Nencioli, F., Petrenko, A.A., Doglioli, A.M., (2016). Diagnosing cross- shelf transport along
963 an ocean front: An observational case study in the Gulf of Lion, Journal of Geophysical
964 Research Oceans, 121, 7218-7243.
965
966 New, A. L. (1988). Internal tidal mixing in the Bay of Biscay. Deep-Sea Research, 35(5), 691–
967 709, doi:10.1016/0198-0149(88)90026-X
968
969 Pauly, D., Christensen, V., Guénette, S., Pitcher, T. J., Sumaila, U. R., Walters, C. J.,Watson.,
970 R., Zeller, D., (2002). Towards sustainability in world fisheries, Nature 418: 689–695,
971 http://doi.org/10.1038/nature01017
972
973 Peliz, A., Santos, A., Oliveira, P., and Dubert, J., (2004). Extreme cross-shelf transport induced
974 by eddy interactions southwest of Iberia in winter 2001, Geophysical Research Letters, 31,
975 L08301, doi:10.1029/2004GL019618
976
977 Pingree, R. D., Mardell, G. T., and New, A. L. (1986). Propagation of internal tides from the
978 upper slopes of the Bay of Biscay. Nature, 321(6066), 154–158. doi:10.1038/321154a0
979
980 Pingree, R.D.,and Le Cann, B., (1989). Celtic and Armorican slope and shelf residual currents.
981 Progress in Oceanography 23 (4), 303–338. https://doi.org/10.1016/0079-6611(89)90003-7
982
983 Pingree, R. D. , and Le Cann, B., (1990). Structure, strength and seasonality of the slope
984 currents in the Bay of Biscay region, Journal of the Marine Biological Association of the UK
985 70, 857–885. https://doi.org/10.1017/S0025315400059117
986

Pingree, R.D., and Le Cann, B., (1992a). Anticyclonic eddy X91 in the southern Bay of Biscay, May 1991 to February 1992. Journal of Geophysical Research, 97 (C9), 14,353–14,367. https://doi.org/10.1029/92JC01181

Pingree, R. D., and Le Cann, B. . (1992b). Three anticyclonic Slope Water Oceanic eDDIES (SWODDIES) in the Southern Bay of Biscay in 1990, Deep-Sea Res. Pt. A, 39, 1147–1175. https://doi.org/10.1016/0198-0149(92)90062-X

Pingree, R. D., Sinha, B., and Griffiths, C. R. (1999). Seasonality of the European slope current (Goban Spur) and ocean margin exchange, Continental Shelf Research, 19, 929–975, doi:10.1016/S0278-4343(98)00116-2

Pingree, R. D., and Garcia-soto, C. (2014). Plankton blooms , ocean circulation and the European slope current : Response to weather and climate in the Bay of Biscay and W English Channel (NE Atlantic). Deep-Sea Research Part II, 106, 5–22. http://doi.org/10.1016/j.dsr2.2014.07.008

Piola, A. R., Mart´ınez Avellaneda, N., Guerrero, R. A., Jardon, F. P., Palma, E. D., Romero, S. I. (2010). Malvinas-slope water intrusions on the northern Patagonia continental shelf, Ocean Sci., 6, 345– 359. https://doi.org/10.5194/os-6-345-2010

Porter, M., Inall, M. E., Green, J. A. M., Simpson, J. H., Dale, A. C., and Miller, P. I. (2016). Drifter observations in the summer time Bay of Biscay slope current, Journal of Marine Systems, 157, 65–74. http://doi.org/10.1016/j.jmarsys.2016.01.002

1012 Rubio, A., Caballero, A., Orfila, A., Hernández-Carrasco, I., Ferrer, L., González, M.,
1013 Solabarrieta, L., and Mader, J. (2018). Eddy-induced cross-shelf export of high Chl-a
1014 coastal waters in the SE Bay of Biscay, Remote Sensing of Environment, 205, 290–304.
1015 http://doi.org/10.1016/j.rse.2017.10.037
1016
1017 Reverdin, G., Marié, L., Lazure, P., d'Ovidio, F., Boutin, J., Testor, P., Martin, N., Lourenco,
1018 A., Gaillard, F., Lavin, A., Ro- driguez, C., Somavilla, R., Mader, J., Rubio, A., Blouch,
1019 P., Rolland, J., Bozec, Y., Charria, G., Batifoulier, F., Dumas, F., Louazel, S., and Chanut,
1020 J., (2013). Freshwater from the Bay of Biscay shelves in 2009, J. Mar. Syst., 109/110,
1021 Supplement S134–S143, https://doi.org/10.1016/j.jmarsys.2011.09.017
1022
1023 Serra, N., I. Ambar, and D. Boutov (2010), Surface expression of Mediterranean Water dipoles
1024 and their contribution to the shelf/slope-open ocean exchange, Ocean Science, 6(1), 191–
1025 209, doi:10.5194/os-6-191-2010.
1026
1027 Shapiro, G. I., Stanichny, S. V., and Stanychna, R. R. (2010). Anatomy of shelf-deep sea
1028 exchanges by a mesoscale eddy in the North West Black Sea as derived from remotely
1029 sensed data. Remote Sensing of Environment, 114(4), 867–875.
1030 http://doi.org/10.1016/j.rse.2009.11.020
1031
1032 Simpson, J. H. and R. R. McCandliss (2013), " The Ekman Drain": A conduit to the deep ocean
1033 for shelf material, *Ocean Dyn.,* **63**, 1063– 1072. https://doi.org/10.1007/s10236-013-0644-y
1034
1035 Souza, A. J., J. H. Simpson, M. Harikrishnan, and J. Malarkey (2001), Flow structure and
1036 seasonality in the Hebridean slope current, Oceanol. Acta 24(Suppl.), S63–S76.

https://doi.org/10.1016/S0399-1784(00)01103-8

Theetten, S., Vandermeirsch, F., and Charria, G., (2017). BACH1000_100lev-51: a MARS3D model configuration for the Bay of Biscay, SEANOE, https://doi.org/10.17882/43017

Van Aken, H. M., (2002). Surface currents in the Bay of Biscay as observed with drifters between 1995 and 1999. Deep-Sea Research Part I, 49, 1071–1086. https://doi.org/10.1016/S0967-0637(02)00017-1

Xu, W., Miller, P.I., Quartly, G.D., Pingree, R.D., (2015). Seasonality and interannual variability of the European slope current from 20 years of altimeter data compared with in situ measurements. Remote Sensing of Environment 162, 196–207. http://dx.doi.org/ 10.1016/j.rse.2015.02.008.

Yelekçi, Ö., Charria, G., Capet, X., Reverdin, G., Sudre, J., and Yahia, H. (2017). Spatial and seasonal distributions of frontal activity over the French continental shelf in the Bay of Biscay. Continental Shelf Research, 144, 65–79. http://doi.org/10.1016/j.csr.2017.06.015

Zhang, W. G., and G. G. Gawarkiewicz, (2015): Dynamics of the direct intrusion of Gulf Stream ring water onto the Mid- Atlantic Bight shelf. Geophysical Research Letters, 42, 7687–7695, doi:10.1002/2015GL065530.

Zhang, J., X. Guo, L. Zhao, Y. Miyazawa, and Q. Sun, (2017). Water exchange across isobaths over the continental shelf of the East China Sea. Journal of Physical Oceanography, 47, 1043–1060, https://doi.org/10.1175/JPO-D-16-0231.1.

Zhao, L., and X. Guo (2011), Influence of cross-shelf water transport on nutrients and phytoplankton in the East China Sea: A model study, Ocean Science, 7, 27–43, doi:10.5194/os-7-27-2011.

Zhou, F., G. Shapiro, and F. Wobus (2014). Cross-shelf exchange in the northwestern Black Sea, Journal of Geophysical Research Oceans, 119, 2143–2164, doi:10.1002/2013JC009484.

Zhou, F., H. Xue, D. Huang, J. Xuan, X. Ni, P. Xiu, and Q. Hao, (2015). Cross-shelf exchange in the shelf of the East China Sea. Journal of Geophysical Research Oceans, 120, 1545–1572, doi:10.1002/ 2014JC010567.